ALMA MATER STUDIORUM · UNIVERSITY OF BOLOGNA

School of Science
Department of Physics and Astronomy
Master's Degree in Physics

SYNTHESIS AND CHARACTERISATION OF METAL HYDRIDES FOR HYDROGEN STORAGE APPLICATIONS

Supervisor: **Submitted by:**

Prof. Luca Pasquini   **Evans Pericoli**

Academic Year 2022/2023

Abstract

Considering the direction taken for a more sustainable energetic framework, hydrogen could play a crucial role as an energy carrier. One key point relies on the storage technology deployed, which spans from state-of-the-art cryogenic or high-pressure solutions to solid-state storage systems.

Thermodynamic and kinetic characterisations, when coupled with structural and morphological analysis, allow us to perform convenient stoichiometric tailoring for cheap, sustainable, fast and secure hydrogen storage systems, resulting in a high-performance material that meets the required operative conditions.

The present work exploits the volumetric measurements performed on a Sievert's apparatus coupled with powder XRD, SE-SEM and EDX-SEM analysis to characterise the sorption properties of hydride-forming metals.

The first part of the project consisted of the calibration of a Sievert's apparatus, modelling its behaviour in pressure and temperature ranges and characterising reference hydrides such as $PdH_{0.6}$, $LaNi_5H_6$ and Hydralloy C5 (TiZrMnVFe), well-known for their excellent kinetic properties.

Furthermore, the novel $TiFe_{0.9}Ni_{0.1}$ alloy has been synthesised, deploying the arc melting technique to explore the concept of elemental substitution for tailoring the thermodynamic properties of the hydride. Nickel substitution in arc-melted $TiFe$ potentially improves the kinetic and thermodynamic properties of the compound, deploying non-toxic and earth-abundant materials. Intense studies have been carried out in the literature on TiFe substitutions, with Ni being an intriguing candidate to reach fast kinetics, good cyclability and low plateau pressures.

The comprehensive exploration of elemental substitution in AB intermetallic compounds represents a potential direction for future investigations, seeking a deeper understanding of the metal-hydrogen interaction to optimise the microscopic properties of solid-state storage materials.

Contents

5

List of Tables

6

List of Figures

Introduction

The need for a game-changer technology in the energetic world has brought back attention to hydrogen as an energy carrier due to its unrivalled potential for sustainable power applications [1]. Hydrogen shows the highest gravimetric energy density (three times larger than gasoline, $33kWh/kg$ vs $12kWh/kg$) among all energy vectors. When deployed in a fuel cell, it simply produces water as waste. Furthermore, its versatility in generating a variety of chemical compounds with other elements provides a variety of feasible properties to be explored, some of these useful in the energetic framework [2].

Unfortunately, one of the major limitations in deploying hydrogen as an energy carrier relies upon the storing technology adopted: because of the low critical point for H_2 gas ($33.2K$), the volumetric density is too small (70 kg$H_2 m^{-3}$) compared with fuels such as gasoline or methane. An example is provided by the current high-pressure tanks deployed in commercial fuel cell electric vehicles (FCEV), which offer a modest 1.3 kWh/L of energy density at 70 MPa against the 8.8 kWh/L of gasoline [1], making H_2 unfeasible for light-vehicles road transportation.

In the Net Zero Scenario, deploying low-emission hydrogen and hydrogen-based fuels will lead to modest reductions in CO_2 emissions in 2030. The contribution of hydrogen technologies is significantly lower than the ones of other key mitigation measures, such as the deployment of renewables, direct electrification and behavioural change. However, hydrogen and hydrogen-based fuels can play a crucial role in sectors where emissions are hard to abate and where other mitigation measures may not be available or would be problematic to implement. Hydrogen's contribution becomes more significant in the long term as hydrogen-based technologies mature [3].

Furthermore, regarding road transport, battery electric vehicles are more efficient and developed than hydrogen fuel cell electric vehicles (FCEVs). However, hydrogen scales up faster in road transport in the medium term than in shipping and aviation since FCEV technology is further advanced, especially in heavy-duty trucks, representing a feasible alternative to fossil fuels and EVs [3].

One possible direction that offers further investigations would consist of developing and improving a sustainable technology to store hydrogen with solid-state devices. It is possible to characterise these devices with the so-called Pressure-Composition-Isotherms (PCIs), resulting in a profound knowledge of the thermodynamic parameters describing the materials. Hydride's entropy and enthalpy of formation can be tuned to match the required operative standards in terms of temperature, pressure, maximum capacity, and cyclability, resulting in a complex material adequate for hydrogen storage.

The present work aims to discuss the theoretical background underneath the metal-hydrogen interaction to understand the crucial aspects to investigate when synthesising metal hydrides for hydrogen storage applications and to present the results of some characterisations performed on well-known and novel stoichiometry hydrogen-sorption materials. In Chapter 1, the theoretical framework of solid-state storage through metal hydrides is depicted. Chapter 2 shows the experimental method carried out during the project. In Chapter 3, the experimental results and their analysis and interpretation are presented.

Chapter 1

Metal hydrides

1.1 Hydrogen, applications and storage technologies

In order for the hydrogen economy to become competitive with fossil fuels and other renewable sources, it is vital for the "hydrogen cycle" (Figure 1.1) to be self-sustained. The general idea could be to couple an electrolyser to a solar cell, thus favouring hydrogen production without any costs, then store the surplus for further use and finally deploy it in a fuel cell.

Currently, half of the hydrogen available is produced by natural gas (47 %), primarily via steam methane reforming, while 30 % derives from oil, 19 % from coal and only 4 % from water electrolysis [4].

Among the hydrogen production techniques, electrolysis is definitely the most efficient (compared with thermal dissociation of H_2O). At ambient pressure and temperature conditions, water splitting requires $1.48\,V$, thus a minimum energy of $39.7\,kWhkg^{-1}$ with an energy consumption of $47kWhkg^{-1}$ (efficiency of 82%) [5].

The interest in this element as an energy carrier relies upon its use as fuel in fuel cells (FCs) such as proton-exchange membrane fuel cells (PEMFC). These devices have a capacity range of 200 kW - 2 MW, to be compared with a standard internal combustion engine (diesel) that spans in the 500 kW - 50 MW interval, which, on the other hand, shows a much smaller efficiency (35 % diesel engine vs the 40 - 85 % for FCs). These parameters, along with capital cost, make fuel cells a valid competitor in the energetic framework, tripling the efficiency of windmills and solar cells [6].

The functioning idea behind a fuel cell is simple: two hydrogen and two oxygen molecules react to form two water molecules and energy (electricity and heat) via an electrochemical reaction reversed with respect to the electrolysis reaction. In
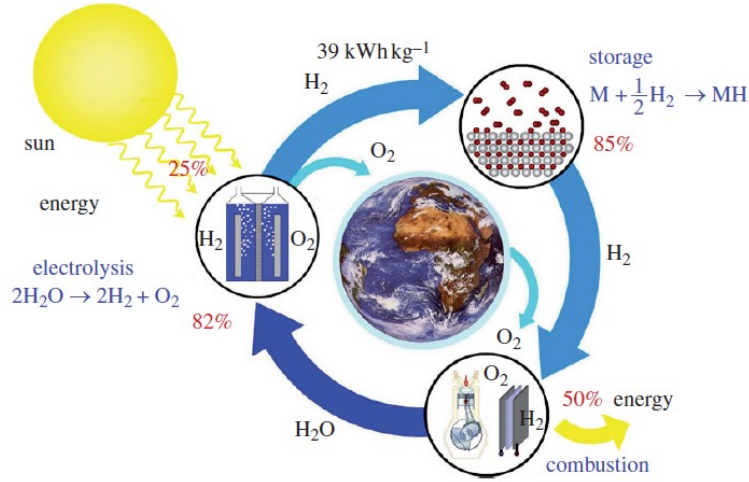
Figure 1.1: Self-sustained hydrogen cycle: the surplus sun energy converted through photovoltaic cells is deployed to power an electrolyser that produces hydrogen by water splitting. Then, hydrogen is stored and used in a fuel cell, producing electric energy and water as waste [5].

formula:

$$2H_2(g) + 2O_2(g) \rightleftharpoons 2H_2O + energy. \tag{1.1}$$
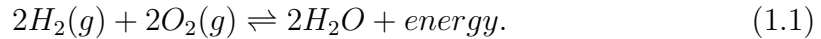
At the anode, hydrogen is oxidised into protons and electrons, while oxygen is reduced at the cathode to oxide species and reacts to form water. Depending on the electrolyte, protons or oxide ions are transported through an ion-conductor electron-insulating solution while electrons travel through an external circuit to deliver electrical power [6].

The most critical part of the production - storage and transport - final application relies on the storage section: once the hydrogen has been produced, possibly in the greenest way by coupling a solar cell to an electrolyser or by directly deploying a photo-electrochemical cell (PEC), it needs to be stored for further undefined usage. Theoretically, $1\,kg$ of hydrogen occupies $11\,m^3$ at ambient temperature and pressure conditions. There are three possible approaches to reducing hydrogen volume: increasing pressure, decreasing temperature, or chemically confining it, reducing molecular oscillations.

The most common storage systems are high-pressure gas cylinders, with a maximum pressure of $20\,MPa$ ($80\,MPa$ for the state-of-the-art composites) and a volumetric density of $36\,kgm^{-3}$. These systems suffer from one major limitation (apart from the tremendously high operative pressures): because of the tensile strength of the materials, an increase in the applied pressure results in a larger volumetric density but a lower gravimetric density.

Liquid hydrogen is stored at $21.2\,K$, reaching a volumetric density of $70.8\,kgm^{-3}$, with major limitations concerning the process efficiency and the energy necessary to reduce the boil-off [5].

Hydrogen can be stored in metals that reversibly form hydrides under specific pressure/temperature conditions, which may be suitable for practical applications. This solution offers an enormous advantage regarding the increased volumetric density, with a concurrent decrease in the gravimetric density due to the heavy host metals [1].

Figure 1.2 shows the density profile of metal hydrides, pressurised gas systems and liquid hydrogen storage tanks. Clearly, metal hydrides represent a desirable solution in terms of volumetric density despite the low gravimetric density compared with several high-pressure composite storage systems. In order for these compounds to be competitive with the standard storage systems already deployed, they should be earth-abundant, economically feasible and environmentally friendly. In this sense, the US Department of Energy and the Fuel Cell and Hydrogen Joint Program of the European Energy Research Alliance (EERA) for hydrogen storage materials set some key features that these materials should fulfil [1]:

- A gravimetric density around $5 - 10\,wt\%$ which is reflected in an energy density of $1.6 - 3.2\,kWhkg^{-1}$

- A volumetric density larger than $50\,kgm^{-3}$, corresponding to an energy density larger than $1.6kWhL^{-1}$

- An operational temperature $T^0_{stationary} < 200\,°C$ and $T^0_{transport} < 85\,°C$

- Fast kinetics (3-5 min fill-time)

- Good durability (1500 cycles)

Among the hydrides, the most stable are the ones formed between hydrogen and electropositive elements such as *Sc, Y, La* and *Ac* periods, *Ti* and *V* groups, along with alkali and alkali-earths. Metallic hydrides MH_n are characterised by an interstitial occupation of hydrogen in the octahedral or tetrahedral sites and good stability, except for metals from Group 6 to 11 [7], as shown in Figure 1.3.

Of great interest are the metal hydrides of ternary intermetallic compounds in the form AB_xH_n, where A is a rare-earth (RE), alkaline-earth or early transition metal (ETM) element with high H affinity and B is a late transition metal (LTM) element with low H affinity. The reason behind their promising features lies in the composition: by tailoring the compound stoichiometry, it is possible to obtain the desired thermodynamic parameters which govern the formation of the hydrides and rule the energy involved in the process.
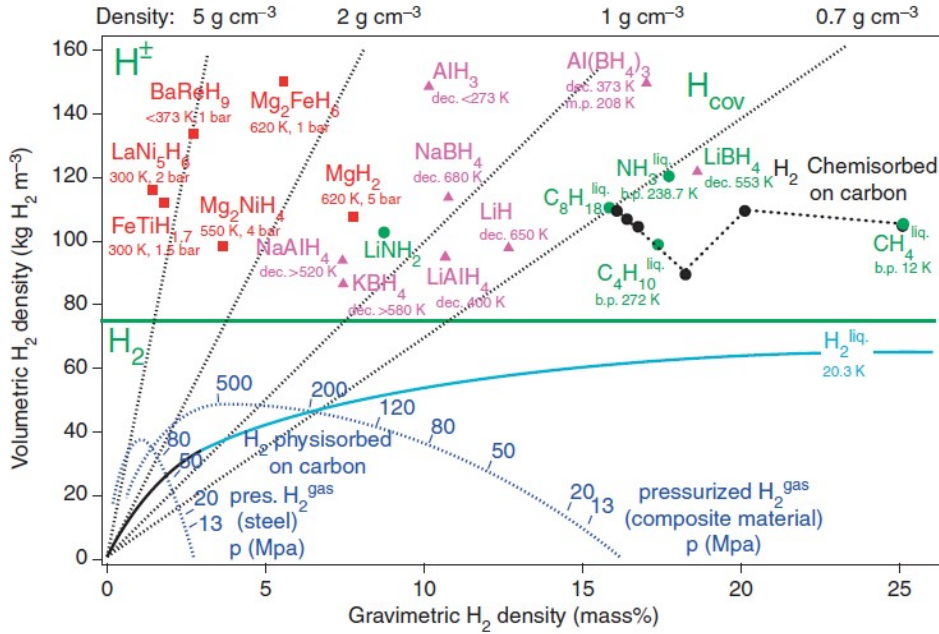
Figure 1.2: Volumetric vs gravimetric density of several storage systems (high pressure and low-temperature tanks compared with metal hydrides). Mg_2FeH_6 exhibits the highest known volumetric density of $150\,kg\,m^{-3}$, while $LiBH_4$ shows the highest gravimetric density of $18\,wt\%$ [7].

1.2 Thermodynamics and compositional tailoring

Figure 1.4 - A shows the energetic profile of molecular and atomic hydrogen when approaching a metallic surface. The atom and the molecule are separated by the dissociative Lenard-Jones potential, and when they are close enough to the interface, physisorption may occur through Van der Waal's interactions. The quantum mechanical states overlapping brings to the Pauli repulsion (orthogonal states) that can be overcome by hybridisation and the formation of bonding and anti-bonding states. In this context, molecular chemisorption is induced on the metal surface, followed by surface diffusion and sub-surface penetration [7].

Subsequently, as reported in Figure 1.4 - B, hydrogen atoms will start diffusing inside the metal, forming a solid solution referred to as $\alpha - phase$ for low concentrations ($H/M < 0.1$).

Figure 1.3: Hydrogen-Element interaction and Allred-Rochow electronegativity. Yellow elements do not form stable hydrides (Group 6 to 11), with the exception of Ni and Pd [7].

1.2.1 Solid solution (α phase)

In this context, the process would be described by the relation:

$$M(s) + 1/2xH_2(g) \rightleftharpoons MH_x(s). \tag{1.2}$$
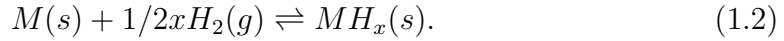
At the equilibrium, the chemical potential of hydrogen in gaseous and metal solution must be equal, following:

$$\frac{1}{2}\mu_{H_2}^{gas} = \mu_H^M, \tag{1.3}$$

where the chemical potential of the ideal gas phase is equal to:

$$\mu_{H_2}^{gas} = \mu_0 + k_B T ln\left(\frac{p_{H_2}}{p_0}\right), \tag{1.4}$$

while the chemical potential of hydrogen inside the metal is:

$$\mu_H^M = \left(\frac{\partial G_H^M}{\partial n_H}\right)_{T,p}, \tag{1.5}$$

20
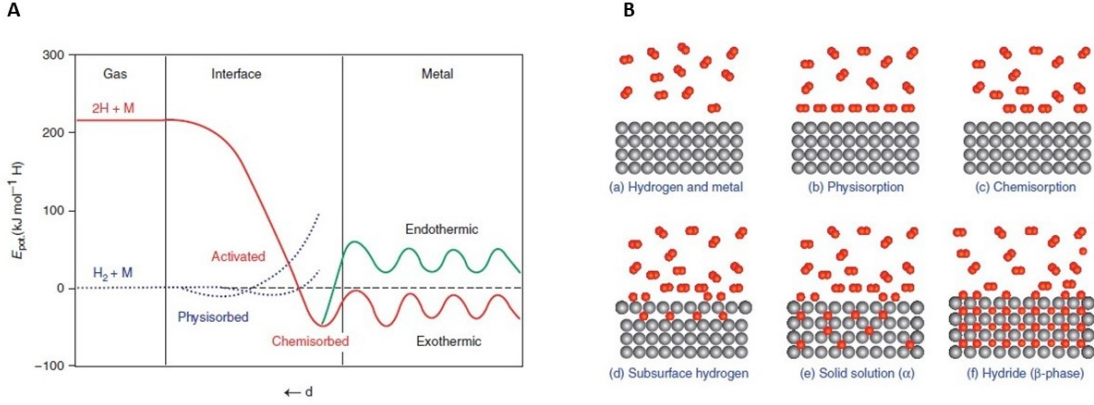
Figure 1.4: Lenard-Jones energy potential for atomic and molecular hydrogen. The dissociation energy on the left, far from the metal surface, is $E_D = -218\,kJmol^{-1}H$. When approaching the metal surface physisorption (Van der Waal's interactions) and chemisorption are induced. The next step would be surface diffusion and sub-surface penetration, followed by diffusion, solid solution and stable hydride formation [7].

$G_H^M = H_H^M + T\left(S_H^{Mconfig} + S_H^{Mexc}\right)$ being the Gibbs free energy of hydrogen in metal, H_H^M its enthalpy and S_H^M its entropy, composed of configurational and excess components due to vibrational and electronic contributions. By developing all the calculations, it is possible to find the chemical potential of hydrogen in metal as:

$$\mu_H^M = \mu_H^{M0} + k_B T ln\left(\frac{c_H}{r - c_H}\right) \tag{1.6}$$

where $\mu_H^{M0} = h_H^M - T s_H^{Mexc}$ is the standard chemical potential, c_H is the hydrogen concentration and $r = N/N_0$ is the number of interstitial sites per atom. By putting together eq. (1.4) and (1.6) it is easy to obtain:

$$\frac{c_H}{r - c_H} = \sqrt{\frac{p_{H_2}}{p_0}}\,exp\left(\frac{-h_H^M - T s_H^{Mexc} - \frac{1}{2}\mu_0}{k_B T}\right). \tag{1.7}$$

In the limit of low concentration ($c_H < 0.1H/M$) and for $r = 1$ (like in Pd), the previous relation can be expressed as:

$$c_H = \sqrt{\frac{p_{H_2}}{p_0}}\,exp\left(\frac{-h_H^M - T s_H^{Mexc} - \frac{1}{2}\mu_0}{k_B T}\right), \tag{1.8}$$

known as Sievert's law. From these relations, it is possible to extract the enthalpy variation from gas to metal state in absorption, known as the heat of solution.

All the previous mathematical treatments can be found in the Physical Metallurgy book by Kirchheim and Pundt [8]. A more general and comprehensive description is provided by Fukai [9].

1.2.2 Lattice expansion

By following Kirchheim and Pundt argumentations [8], it is easy to observe that hydrogen solution in the interstitial sites of the metal causes host metal atom displacement and lattice expansion, which is reflected in the presence of a strain or stress described by the volume change per hydrogen atom relative to the metal atom volume $\frac{\Delta\nu}{\Omega}$. Therefore, the variation of the total volume of the metal, containing N atoms of volume Ω, is equal to:

$$\frac{\Delta V}{V} = \frac{n_H \Delta\nu}{N\Omega} = c_H \left(\frac{\Delta\nu}{\Omega}\right). \tag{1.9}$$

Therefore, the variation in the metal volume is directly related to the hydrogen concentration c_H, provided that defect density is small and constant. If hydrogen randomly occupies interstitial sites (a reasonable assumption), it is straightforward to conclude that crystal expansion would be isotropic, allowing to reduce eq. (1.9) to a one-dimensional relation (neglecting higher orders for small volume variations):

$$\frac{\Delta V}{V} = 3\frac{\Delta L}{L} + O\left(\left(3\frac{\Delta L}{L}\right)^2\right) + ... \tag{1.10}$$

or, equivalently,

$$\frac{a_H^3 - a_0^3}{a_0^3} = c_H \left(\frac{\Delta\nu}{\Omega}\right) = 3\frac{\Delta a}{a_0} + O\left(\left(3\frac{\Delta a}{a_0}\right)^2\right) + ..., \tag{1.11}$$

where $\Delta a/a_0$ can be easily determined by X-ray or neutron diffraction.

Experiments show that, up to a concentration of $0.7H/M$, lattice expansion is independent of the host metal's initial volume. The difference in the volume variations regarding several atomic species depends on the type of bonding: for d-metals could be the formation of local bonding states with the consequent depletion of anti-bonding states, while for lanthanide metals could be the charge transfer from metal to hydrogen that enlarges the total volume occupied by the latter resulting in an increased value of $\Delta\nu$ [9].

1.2.3 Hydride formation (β-phase)

Lattice expansion typically leads to a decrepitation of the brittle host metals, resulting in a powder with average particle size in the $10 - 100\,\mu m$ range [7]. Once

the metal has reached a saturation solubility with concentration c_α, a hydride $\beta - phase$ starts to grow inside the metal, associated with the chemical reaction of the hydrogen with metal atoms:

$$\frac{1}{c_\beta - c_\alpha}MH_{c_\alpha} + \frac{1}{2}H_2 \rightleftharpoons \frac{1}{c_\beta - c_\alpha}MH_{c_\beta}. \tag{1.12}$$
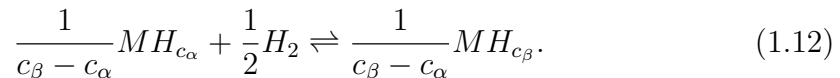
At this point, a miscibility gap forms due to the impossibility of the α phase to mix completely with the β phase. At the equilibrium, the Gibbs free energy must reach a minimum:

$$\Delta G_H^{\alpha-\beta} = \Delta H_H^{\alpha-\beta} - T\Delta S_H^{\alpha-\beta} = G^{0,\beta} - G^{0,\alpha} - RTln\left(\frac{p_{H_2}}{p_0}\right) = 0, \tag{1.13}$$

where $\Delta G_H^{\alpha-\beta}$ is the Gibbs free energy of hydride formation, associated with the coexistence of the α and β phase. From the previous equation, it is possible to obtain the well-known Van't Hoff equation describing the relation between the pressure at the equilibrium condition between the two coexisting phases and the intrinsic thermodynamic parameters:

$$ln\left(\frac{p_{H_2}}{p_0}\right) = \frac{\Delta H^0}{RT} - \frac{\Delta S^0}{R}. \tag{1.14}$$
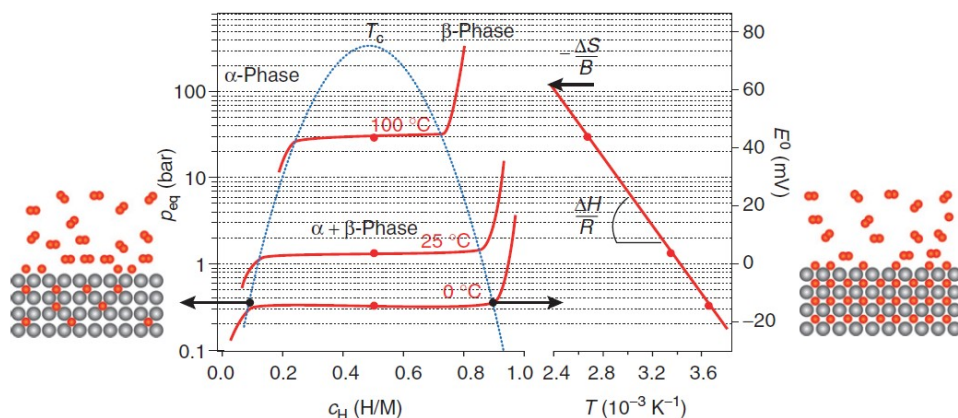
Figure 1.5: Pressure-Composition-Isotherms (PCIs) of a metal hydride. Low H concentrations correspond to the solid solution ($\alpha - phase$), while higher concentrations are associated with the hydride formation ($\beta - phase$). The coexisting region, characterised by a miscibility gap, is associated with a constant value of hydrogen pressure. On the right, Van't Hoff plot reporting $ln(p)$ vs $1/T$, from which the hydride thermodynamic parameters can be extracted [7].

Figure 1.5 shows the profile of the hydrogen pressure related to its concentration inside the metal. It is easy to see that, for low H concentrations, the pressure follows a square profile, while it stabilises when reaching the miscibility gap.

Each curve in the diagram represents a Pressure-Composition-Isotherm (PCI), characterised by a plateau pressure which can be used to identify both enthalpy and entropy of formation in the Van't Hoff plot reported on the right. By increasing temperature, the concentration interval for the flat plateau decreases up to a single point, corresponding to the pressure-composition coordinate at the decomposition temperature:

$$T_{dec}\Big|_{p=p_0} = \frac{\Delta H^0}{\Delta S^0}, \tag{1.15}$$

above which the phases are fully mixed, and the miscibility gap disappears.

While the enthalpy term in eq. (1.14) characterises the metal-hydrogen bond stability, the entropy of formation is mostly related to the molecular dissolution of hydrogen into the $\alpha - phase$, and its typical value is $\Delta S \approx -130\,JK^{-1}mol^{-1}$.

A topic of debate in the scientific community is represented by hysteresis between the absorption/desorption plateaus in the PCIs curve. This phenomenon is typically related to the formation and migration of dislocations at the $\alpha - \beta$ interfaces. Dislocations may be formed when there's an excess energy contribution caused by the elastic strain energy between the interfaces. This dissipative energy is reflected as a hysteresis in the loading/unloading process [8]. Furthermore, Schwartz and Katchaturyan [10] showed that hysteresis may also be generated at coherent metal/hydride boundaries even after several loading/unloading cycles when dislocations could not play a significant role anymore. In particular, the stress at the coherent interface between β-precipitates and metal-matrix produces a macroscopic thermodynamic energy barrier that results in an increment of the chemical potential during hydride formation and a reduction of the former in the case of hydride decomposition. This condition is manifested as a reduction in the desorption equilibrium pressure and an increment in the absorption one compared to the theoretical value expected by the Van't Hoff equation.

To conclude, it is noteworthy to highlight that the entropy of formation brings a significant amount of heat evolution $\Delta Q = T\Delta S^0$, determining the exothermic character of the reaction during absorption. The same energy has to be provided in the desorption process due to the endothermic nature of the event [5].

1.2.4 Hydride stability and stoichiometric tailoring

The reason that makes AB_n intermetallic compounds so appealing for storage applications can be attributed to their unique structure and interaction with hydrogen atoms. Since they are capable of forming complex yet ordered structures such

as Laves or Heusler phases, hydrogen accommodation is positively influenced. In this context, Lundin et. al [11] developed an empirical geometric model introducing a theoretical framework to understand and predict the behaviour of intermetallic compounds when forming hydride phases. The model analyses the effects of atomic arrangement on sorption properties: considering the size and geometry of the interstitial sites, the electronic structure of the metal atoms and the interaction between hydrogen atoms and lattice metal, it depicts the possible thermodynamic features of the compound. More specifically, a correlation has been found between the enlargement of the unit-cell volume (reflected in a larger interstitial site) and a reduction of the equilibrium pressure (shifting PCIs to lower values). A comprehensive analysis would require *ab initio* calculations to account for electronic band structure.

Concerning hydride stability, the Miedema model states that the more stable the intermetallic compound, the less stable the corresponding hydride since hydrogen needs to fit in a partially broken-bond environment to interact chemically with the metal atoms [7]. Furthermore, experimental observations bring to the conclusion that hydrogen stability in an interstitial site corresponds to the weighted average of the corresponding binary hydrides stability of the neighbouring metallic atoms:

$$\Delta H\Big([A_a B_b]H\Big) = \Delta H\Big(A_m H_{xa/a+b}\Big) + \Delta H\Big(B_n H_{xb/a+b}\Big). \qquad (1.16)$$

Therefore, when dealing with a transition metal A with a high H affinity, it is reasonable to assume that hydrogen will surround the former, isolating it from the less attractive B metal. The generalised form of eq. (1.16) accounting for AB_n compounds with $n < 5$ is:

$$\Delta H\Big([ABn]H_{2m}\Big) = \Delta H\Big(AH_m\Big) + \Delta H\Big(B_n H_m\Big) - \Big(1 - F\Big)\Delta H\Big(AB_n\Big), \quad (1.17)$$

$(1 - F)$ being the number of broken $A - B$ bonds due to interstitial hydrogen.

Therefore, one considerable advantage from the technological point of view stands in the possibility of tuning the enthalpy and entropy of formation by simply choosing the proper intermetallic compound or by acting on an AB_n compound through elemental substitution following the guidelines of the geometric model (when applicable), thus tailoring the stoichiometry of the alloy to obtain the desired thermodynamic parameters. Intense studies have been carried out to explore the effects of substitutions on *TiFe* to improve hydrogen storage properties [12]. Dematteis et al. observed that substitution could significantly lower the plateau pressure (a phenomenon that finds its reasons in the geometric model), inducing a smoothing effect, levering plateau pressure and maximising the reversible capacity of the hydride.

1.2.5 Lattice gas model

A good description of the hydrogen behaviour inside a metal is provided by the lattice gas model defined by T.D. Lee and C. N. Yang [7], in which a monoatomic gas interacts in a potential of the form:

$$U(r) = \sum_{i,j} U\Big(|r_i - r_j|\Big), \qquad (1.18)$$

r_i being the position of the ith atom in the crystal. Since we expect hydrogen atoms not to compenetrate but to interact in a short range, the potential has to fulfil the following properties:

- U(r) $= +\infty$ for $r < a$ (a being the radius of each atom)

- U(r) $= 0$ for $r > b$ (limited range)

- U(r) can't be $-\infty$

The energy of the system of hydrogen atoms dissolved in a metal is therefore provided by:

$$E = N_H \epsilon_0 + N_{HH}\epsilon, \qquad (1.19)$$

where N_H is the number of hydrogen atoms with energy ϵ_0, while N_{HH} is the number of interacting nearest-neighbours hydrogen atoms (provided by the Ising model) with energy ϵ. In the Bragg and Williams approximation, the H-H interaction is weak, resulting in no short-range order around the hydrogen sites and a total energy of:

$$E = N_H \epsilon_0 + \frac{\epsilon}{2} n \frac{N_H^2}{N}, \qquad (1.20)$$

where n defines the number of nearest-neighbours interstitial sites and N is the total number of available sites.

Starting from the energy and once derived the partition function for the system, it is possible to obtain an expression for the Helmholtz free energy:

$$F = k_B T N[c_H ln(c_H) + (1 - c_H)ln(1 - c_H)] + N[\epsilon_0 c_H + \frac{\epsilon}{2} n c_H^2], \qquad (1.21)$$

where c_H is the hydrogen concentration in the metal. Notably, the concentration may differ from the value x of a metal hydride MH_x since the number of interstitial sites N may differ from the number of atoms. From the previous equation, it is easy to evaluate the chemical potential:

$$\mu_H(c_H, T) = \frac{1}{N}\frac{\partial F}{\partial c_H}\Big|_{T,V} = k_B T ln\Big(\frac{c_H}{1 - c_H}\Big) + \epsilon_0 + \epsilon n c_H. \qquad (1.22)$$
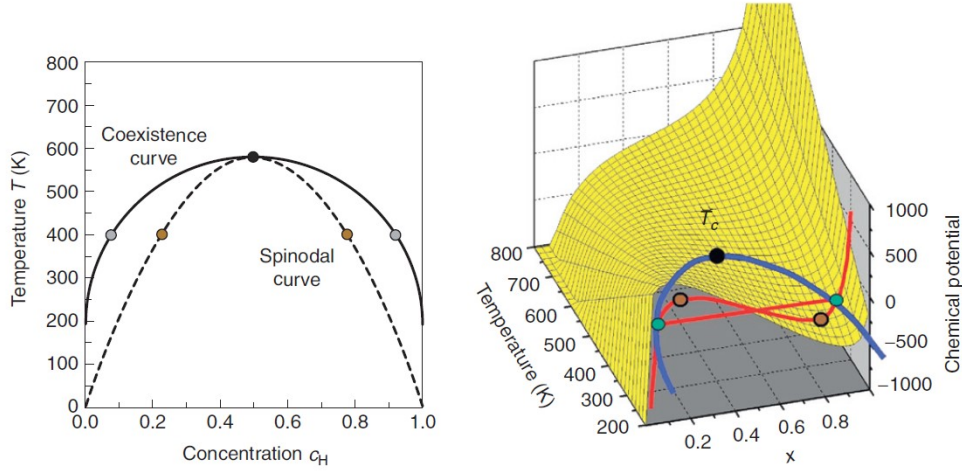
Figure 1.6: Temperature-composition-chemical potential diagram for $\epsilon n = -0.2 eV$. The diagram on the left shows the coexistence curve characterised by an infinitely sharp solubility at $c_H = 0, 1$ and the spinodal curve, which instead shows a softer profile on the extremes of the interval [7].

At the thermodynamic equilibrium, the chemical potential of the gas and the solid solution must be equal, resulting in Sievert's law, already derived in eq. (1.8).

When two coexisting phases are present, with concentration c_α and $c_{\alpha'}$ equal to:

$$k_B T ln\left(\frac{c_i}{1-c_i}\right) + \epsilon n\left(c_i - \frac{1}{2}\right) = 0, \qquad (1.23)$$

it is possible to establish the dissociation pressure following eq:

$$k_B T ln\left(\frac{p_{diss}}{p_0(T)}\right) = 2\epsilon_0 + \epsilon n - \epsilon_b \qquad (1.24)$$

where ϵ_b is the binding energy of a hydrogen molecule.

The coexisting curve, symmetric in $c_H = 1/2$, resulting from the presence of two phases, will present a critical temperature obtained by differentiating eq. (1.23):

$$T_c = -\frac{\epsilon n}{4k_B}. \qquad (1.25)$$

These results can be visualised in Figure 1.6. The temperature-composition diagram is typical of a binary system exhibiting a miscibility gap.

Phase transformations occur whenever the variation in the free energy brings the system to a more stable state. The direction of the process, in this case, is strongly related to the hydrogen concentration value: in the region within the miscibility gap but outside the spinodal line, a bulk free energy has to be overcome

to observe the formation of solute-rich phases, something which typically happens in the presence of solute atoms saturation in the region, such as the nucleation of the solute-rich phase in a region of atomic dimension. This is the case of a discontinuous phase transformation, which requires a variation in the concentration which is large in degree but small in extent. Conversely, in the region identified by the spinodal line, the system is initially unstable, no energy barrier appears, and an infinitesimal variation in the concentration triggers the transformation, which can occur over a large region simultaneously. A typical example is provided by the spinodal decomposition [13].

1.3   Kinetic model for hydrogen sorption

1.3.1   Sorption mechanisms

Thermodynamics is not able to describe the evolution of the metal-hydrogen interaction. Thus, a kinetic model is necessary, which contemplates all the elementary processes reported in Figure 1.4 - B. Each one may be the rate-determining step (RDS) or even a combination of more:

- gas diffusion to the metallic interface

- H_2 chemisorption

- surface diffusion or subsurface penetration of H

- H diffusion in the $\alpha - phase$

- chemical interaction and nucleation and growth of $\beta - phase$.

Typically, the hydrogen chemisorption process requires an energy barrier to be overcome (activation energy E_A), making this interaction the RDS of the whole process. Apart from some highly-reactive metals (Pd), an activation treatment is necessary to induce faster chemisorption at the interface (something that will be discussed in the following sections) or the addition of a catalyst to lower the activation barrier [1].

Once the hydrogen atoms have permeated the metallic surface, they start diffusing through defects as preferential pathways. The diffusion in the solid solution is typically a fast process, but it can be significantly influenced by the hydride phase formation. Therefore, once the $\beta - phase$ starts to nucleate and grow, H diffusion may become the RDS.

Nucleation and growth of β clusters occur when the solid solution saturates, and small particles begin to aggregate inside the $\alpha - phase$. It is noteworthy to say

that the process is associated with an increase of the elastic strain ϵ, and it strongly depends on the $\alpha - \beta$ interface free energy γ. More specifically, the nucleation rate is proportional to the Gibbs free energy of the critical nucleus through $e^{-\Delta G_C}$, where $\Delta G_c \propto \gamma^3$. Since coherent interfaces (whose development is favoured for small nuclei due to the high interface/volume ratio) are associated with a high interface free energy γ and low strain ϵ while incoherent interfaces (which instead develop when there's nuclei growth) have a small γ and large ϵ, the competition between interface free energy and strain determines the type of interface prevailing at the different growth stages [1] [14]. Since the development of the M-H interface requires atomic incorporation (which is a thermally activated process), its motion may become the *RDS*, dealing with an interface-limited rate-determining step.

1.3.2 Johnson-Mehl-Avrami-Kolmogorov (JMAK) model

The complexity of the subsequent or competitive processes occurring during hydrogen sorption brought to the development of a model based on nucleation and growth events. The *JMAK* model is a phenomenological approach describing the kinetics of isotherm phase transformations carried by nucleation and growth. It can be applied whenever

- nucleation is a random process in the bulk

- the transformed regions are negligible in extent compared to the bulk

- the nucleation rate is constant, resulting in a homogeneous growth.

The model relates the reaction fraction ξ (associated with hydrogen absorption or desorption) to the rate constant *k(T)* and a reaction order n through:

$$\xi = 1 - e^{-(kt)^n}. \tag{1.26}$$

The Avrami exponent $n = a + bc$ depends on $a = 0$ if nucleation concluded at the beginning of the process or $a = 1$ if the nucleation rate is constant in time, $b = 0.5, 1$ for diffusion-limited or source-limited events and finally on $c = 1, 2, 3$ describing the process dimensionality ($c = 3$ is associated with a *3-D* spherical growth). The linearization of eq. (1.26) brings to:

$$ln\Big(-ln(1-\xi)\Big) = n ln(t) + n ln(k), \tag{1.27}$$

allowing for a straightforward determination of the angular coefficient n and intercept *nln(k)* in a linear fit. Other models may be considered, which nevertheless bring approximatively the same results: the contracting volume model, which relates the reaction fraction to the rate constant through $1 - [1 - \xi]^{1/2} = kt$ and

describes the case of a *2-D* growth with constant interface velocity, surface-limited model, which depicts the situation of dissociation/recombination as RDS. In the latter case, if the energy barrier associated with the process does not change in time, the kinetics may be expressed as $\xi = kt$. The previous section followed the argumentations proposed by [1]. A comprehensive and structured approach can be found in [15].

1.3.3 The Arrhenius equation

Once the general formula for hydrogen kinetics has been identified, finding a relation like

$$f(\xi) = kt, \tag{1.28}$$

where $f(\xi)$ has a different structure for each RDS, it is possible to relate the rate constant $k(T)$ to the temperature in the system by following the well-known Arrhenius equation:

$$k(T) = k_0 e^{-\frac{E_A}{RT}}, \tag{1.29}$$

k_0 being the pre-factor rate constant, R the ideal gas constant, T the temperature of the system and E_A the activation energy associated with the RDS.

A more generalized version of the previous equation would be:

$$k(T) = k_0 e^{-\frac{E_A}{RT}} h(r, r_0) g(p, p_{eq}), \tag{1.30}$$

where $h(r, r_0)$ contemplates the dependence of $k(T)$ on the particle radius in the nucleation process and a $g(p, p_{eq})$ accounts for a dependence on the gas pressure [16].

Since the driving force for the hydride formation (nucleation and growth phase transition) strongly relies on the hydrogen concentration, it is straightforward to find a connection between the rate constant and the macroscopic parameter associated with c_H: the gas pressure. More specifically, the higher the difference (in absolute value) of the gas pressure compared with the equilibrium condition set by the material thermodynamics, the larger the driving force determining the kinetic event, both in absorption and desorption. The structure of $g(p, p_{eq})$ may depend on the pressure range under analysis and on the element involved in the process, spanning from a linear difference $g(p, p_{eq}) = p - p_{eq}$ and going to more structured dependencies such as $g(p, p_{eq}) = p^{1/2} - p_{eq}^{1/2}$ or $g(p, p_{eq}) = p/p_{eq}$ [16].

Concerning the particle radius instead, it can be demonstrated that diffusion increases as particle radius decreases, following a $\frac{1}{r_0^2}$ trend. Regarding chemisorption and subsurface penetration, a similar trend may be identified, resulting in a dependence of the rate constant over $\frac{1}{r_0^n}$ [16].

30

1.4 Synthesis techniques

This section is dedicated to a brief description of the theoretical framework of the synthesis techniques deployed during the experiments.

1.4.1 Ball Milling

Mechanochemical synthesis, in the form of Mechanical Milling (MM) or Mechanical Alloying (MA), represents a versatile and efficient technique to synthesize a reactive alloy for hydrogen sorption. The process is based on the repeated fracture and welding of the elemental particles constituting the powder due to collisions with hard spheres, which results in a reduction of particle size and atomic interdiffusion through the generated defects [2]. The main difference between MM and MA is that in the former, the milling is carried out onto an already-alloyed compound, while the latter is used to alloy different elemental powders.

One of the most significant advantages of mechanochemistry is the possibility of reaching super-saturated solid solutions even when dealing with positive heat of mixing systems (therefore, immiscible compounds at the thermodynamic equilibrium). The solubility extension feature strongly depends on the milling time and the intensity of the collisions.

Another attractive aspect of this technique is that the process can be carried out in an inert (Ar, N_2) environment or under a high-pressure H_2 atmosphere. In the former conditions, surface oxidation and poisoning are prevented, increasing the kinetic properties of the alloy. In the case of a hydrogen environment, chemical reactions are induced by the energy generated by the collisions, resulting in already-formed hydrides.

1.4.2 Arc Melting

Electric Arc Furnace (EAF) is a furnace capable of alloying several grams of elemental compounds by means of an electric arc. The arc is typically generated in the Ar atmosphere through a high-current generator, which can deliver currents of the order of hundreds of A on a W/W:La electrode. The maximum operating temperature is 3500 °C, sufficient to melt any metal. The melting chamber typically consists of a water-cooled copper crucible in which the elemental rods, clamps, or foils are placed before the procedure.

The controlled environment is ensured by several vacuum cycles through a turbo-molecular pump, the deployment of Argon atmosphere during operation, and an initial treatment with a high-affinity O_2 getter (typically Ti), which reduces poisoning during the alloying.

One of the most significant advantages of deploying the arc melting technique relies on the high homogeneity reached after a few melting cycles: the natural convection inside the melted button induced by the high-temperature operation guarantees a more homogeneous synthesis, compared with mechanical alloying and other synthesis techniques.

1.5   Sample activation

Activation is an often necessary treatment carried out to prepare the material for hydrogen chemisorption and diffusion. This peculiar behaviour of the materials to be reluctant to accept hydrogen in the first cycles of interactions may be attributed to a native passivating layer that forms at the material surface [12]. Since a vast group of elements is sensitive to humidity, oxygen or other gases present in the atmosphere, activation is necessary to promote fresh reactive surfaces, which improve hydrogen chemisorption.

In general, the activation procedure should involve high-pressure treatments (for AB compounds like $TiFe$ even 70 bar) starting from room temperature to ensure the complete activation from the beginning. Conversely, thermal annealing can help enhance hydrogen diffusivity and fresh and clean surface promotion.

Decrepitation induced by high-pressure and temperature treatments decreases hydrogen diffusion distance, causing faster absorption and facilitating stress relaxation in the particles, thus reducing the hydrogen absorption equilibrium pressure. In addition, when the material undergoes expansion and contraction due to hydrogen permeation, a significant volume change is induced, resulting in the crack of the passivating layer and generating defects inside the bulk. More specifically, defects (manifested as microstrains) provide easy diffusion paths and a facilitated motion of the $\alpha - \beta$ interface through the alloy [17].

For what concerns $TiFe$ activation, for instance, it has been demonstrated that annealing could result in the formation of Fe clusters and TiO_2 phases, which might split hydrogen molecules, enhancing chemisorption performances. Furthermore, thermal annealing is widely diffused as a follow-up of Mechanical Alloying (MA), such as Ball Milling (BM), to crack the passivating layer, inducing structural amorphisation and re-crystallisation [12].

1.6   Hydride-forming metals and alloys

This section describes the structure and crystalline phase of the analysed powders. Figure 1.7 shows the possible interstitial sites where hydrogen can land in the hydride phase formation.

1.6.1 Pd

Palladium is a well-known compound for hydrogen storage, appealing for its fast sorption kinetics but quite useless concerning the reversible gravimetric density (less than 1 $wt\%$). It has a copper structure, cubic $Fm\bar{3}m$ space group with lattice parameter equal to 3.92 Å and a density of 12.02 $g\,cm^{-3}$ [18].

Along with Ni, Pd represents the only element in the central group of TM (from 6 to 11) to form a stable hydride ($PdH_{0.7}$). In this phase, hydrogen has high mobility and low charge density, making this element (together with Ni, Ru, Pt) a good hydrogenation catalyst (despite the final unstable hydride phase of Ni or Ru) [7].

1.6.2 LaNi$_5$

$LaNi_5$ belongs to the AB_5 group of materials for hydrogen storage, with a density of 8.60 $g\,cm^{-3}$, an average gravimetric density of 1.5 $wt\%$ and a plateau pressure at *300 K* roughly equal to *2 bar*, fast kinetics and mild thermodynamics conditions for powder activation [19]. It crystallises in the $CaCu_5$ hexagonal structure, space group $P6/mmm$, with coordination of 18 Ni atoms bonded to one La atom. The six shorter bonds are equal to 2.86 Å , while the twelve longer are equal to 3.16 Å [18].

It can be synthesised through BM or arc melting. The latter procedure ensures higher homogeneity even though ball milling typically results in a much more
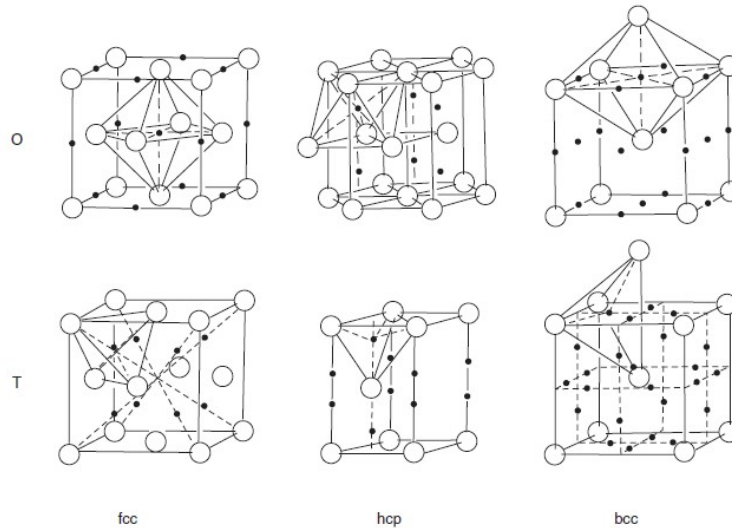
Figure 1.7: Interstitial sites that can potentially host hydrogen atoms in the case of octahedral (O) or tetrahedral (T) cubic and hexagonal structures [9].

nanostructured surface, a desirable feature for an easy activation process.
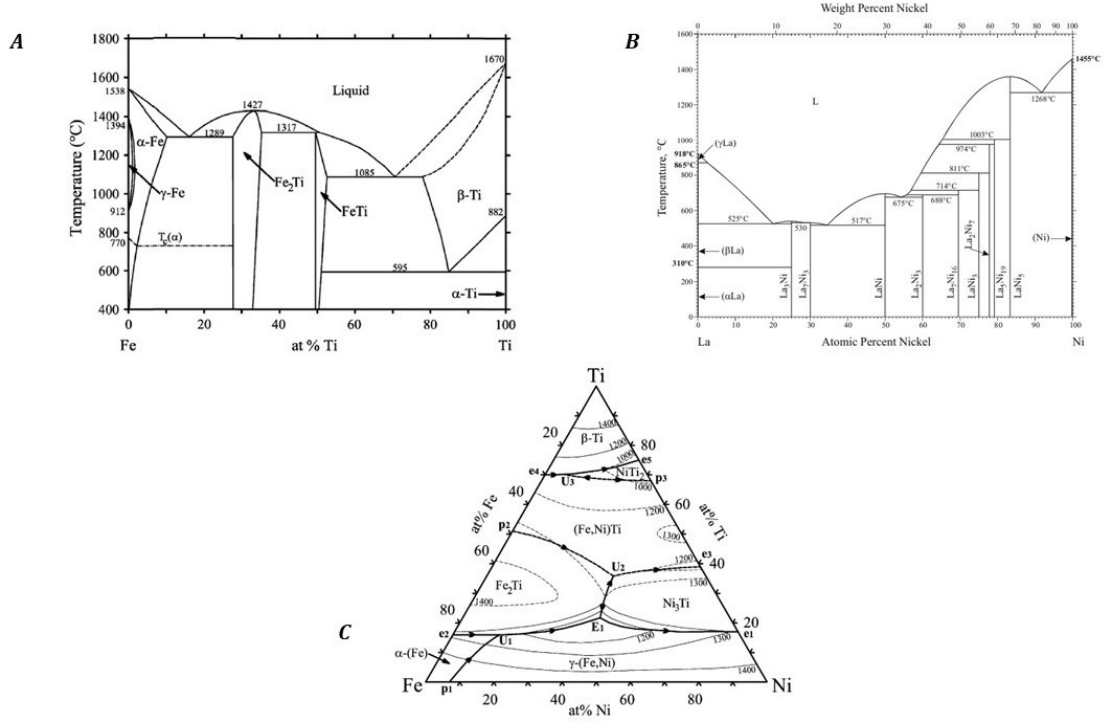
Figure 1.8: **A)** TiFe and secondary phases phase diagram. The TiFe attractive phase for hydrogen sorption can be found in the narrow range (49.7 to 52.5 at%) at the eutectic temperature of 1085 °C [20]. **B)** $LaNi_5$ phase diagram [21]. **C)** Ternary TiFeNi phase diagram [22].

1.6.3 Hydralloy C5

The *Hydralloy C5* ($Ti_{0.95}Zr_{0.05}Mn_{1.46}V_{0.45}Fe_{0.09}$) belongs to the AB_2 intermetallic group of Laves phase metal hydrides. It shares the same *C14* hexagonal structure of $MgZn_2$ [18], it has a density of 6.40 $g\ cm^{-3}$, a gravimetric density of 1.8 $wt\%$, a plateau pressure at 273 K roughly equal to 13 bar in absorption and 7 bar in desorption. It represents an appealing solution for solid-state hydrogen storage due to its versatility in the $-20\ to\ 30$ °C range, relatively fast kinetics and high reversible gravimetric density.

1.6.4 TiFe

$TiFe$ is one of the most studied AB compounds for hydrogen storage, with a reversible gravimetric density of 1.8 $wt\%$, good kinetics and two plateau pressures.

It crystallises in the CsCl cubic structure, space group $Pm\bar{3}m$, lattice constant equal to 2.97 Å [18]. The phase diagram in Figure 1.8 shows that the compound is homogeneous in the range 49.7 to 52.5 $at\% \ Ti$ at the eutectic temperature of 1085 °C [12]. Ti-rich or Fe-rich phases can form by varying the stoichiometric composition, with significant variation in the sorption properties. In particular, it has been observed that $\beta - Ti$ precipitates in $TiFe_{0.905}$ induce hydrogen sorption at room temperature without any activation processes. On the other hand, the $TiFe_2$ phase is typically associated with a significant reduction in the gravimetric density.

The effect of elemental substitution in TiFe alloy has been meticulously investigated by Dematteis et al. [12] due to its enormous potential for solid-state storage applications. With the geometric model, one can potentially forecast the equilibrium pressure value and, therefore, the thermodynamic parameters associated with the compound.

1.6.5 $\mathbf{TiFe_{0.9}Ni_{0.1}}$

Nickel substitution is associated with sorption kinetic and cyclability improvements, a reduction in the hysteresis and in the mono-hydride plateau pressure. Consequently, since the pressure gap between the two plateaus increases, a reduction in the reversible gravimetric capacity is observed. Despite this unfavourable effect, Ni substitution induces an effective decrease of the enthalpy of formation [23], resulting in a reversible gravimetric density below $T = 30$ °C of 1.1 $wt\%$ [12].

$TiFe_{1-x}Ni_x$ shares almost the same TiFe structure (up to x = 0.5 [24]) and can be equivalently substituted in both elements. The precise substitution can be inferred by analysing diffraction peaks [12]. Another noteworthy aspect of deploying nickel relies on the possibility of coupling the substitution with other elements, such as $V, \ Nb, \ Zr$ with positive effects on the hysteresis, kinetic properties and reversible capacity [24].

The combination of these features makes this alloy an intriguing solution for hydrogen storage applications. Indeed, despite the unfavourable conditions for sample activation, the intermetallic compound is made of cheap, earth-abundant materials that effectively store hydrogen in mild pT conditions, meeting several crucial attributes for a storage device.

Chapter 2

Methods

Several approaches exist to measure the concentration of absorbed-desorbed hydrogen in a metal. Two examples could be:

- Thermo-gravimetric measurements, consisting of the accurate evaluation of changes in the sample mass through a highly sensitive balance. Even the sample oxidation could jeopardise the measurement accuracy, along with a lower precision of the measure $(0.1 - 0.3 \ wt\%)$ when overcoming the 2 MPa threshold due to the buoyancy effect [25].

- Volumetric measurements, which instead rely on accurate pressure measurements in a calibrated volume. In fact, hydrogen sorption is associated with slight variations in the sample mass but sensible variations in the chamber pressure. Furthermore, the possibility to access a wider temperature and pressure range without significant loss in accuracy makes this technique more appealing when dealing with hydrogen storage capacity evaluations, PCI and kinetics measurements.

A Sievert's apparatus has been deployed in the present work, exploiting the volumetric measurement technique. The setup was controlled by the LabVIEW-based Hydrogen Sorption Analyser (HSA) software, which allows automatic and manual operations on each instrument component.

The following section is dedicated to the description of the hardware components of the setup and their working mechanism.

2.1 Volumetric measurements and Sievert apparatus

The basic idea in a volumetric measurement is that, in order to observe hydrogen sorption, a specific pressure is set in a portion of the apparatus (where it can't affect the sample) and measured by a pressure gauge, and then a valve (controlled by the software) is opened allowing the hydrogen to flow in the reactor. If the temperature-pressure conditions are favourable for absorption/desorption, the pressure sensor will account for these variations, reporting all data to the software.

Figure 2.1 shows the schematics of the apparatus deployed. From the left, it is possible to see a flow meter controlling hydrogen input in the pipelines, a micrometric valve (MMV1) controlling the hydrogen flow, the pneumatic access valve PV1, a manual valve MV1 connecting the apparatus to a calibrated volume that can be arbitrarily excluded from the measurements, a pressure gauge, the pneumatic exit valve PV3, connected to an expansion volume through the micrometric valve MMV2 (with another pressure gauge) which is linked to a rotary vacuum pump, another pneumatic valve (PV2) connecting the pre-chamber of the setup to the reactor containing the sample holder, a manual valve MV2 to isolate the reactor from the volume between the oven and the pre-chamber and finally the oven.

The whole apparatus has been calibrated by applying the perfect gas equation, providing the exact volume of each section at different temperature conditions.

2.1.1 The calibrated volume

The calibrated volume V_c is an additional component of the setup with known volume and controlled temperature, useful when dealing with different quantities of sample and various experiments: by excluding it from the rest (with the manual valve MV1), one can access a more sensitive range of pressures (smaller amount of hydrogen inside the apparatus), a crucial aspect of the measurements when the mass of the sample is of the order of tens of mg. When performing a kinetic measurement, it is suggested to keep the MV1 valve opened, thus including the volume V_C and increasing the total number of hydrogen moles introduced. In this way, we are sure that the saturation in absorption-desorption is reached before the pressure reaches the equilibrium pressure set by the thermodynamic parameters of the material. Nevertheless, it is not suggested to exclude the calibrated volume when dealing with large amounts of powders. In this case, the mole of sorbed hydrogen wouldn't be sufficient to conclude the process before reaching the equilibrium pressure. It is noteworthy to specify that the calibrated volume dimensions
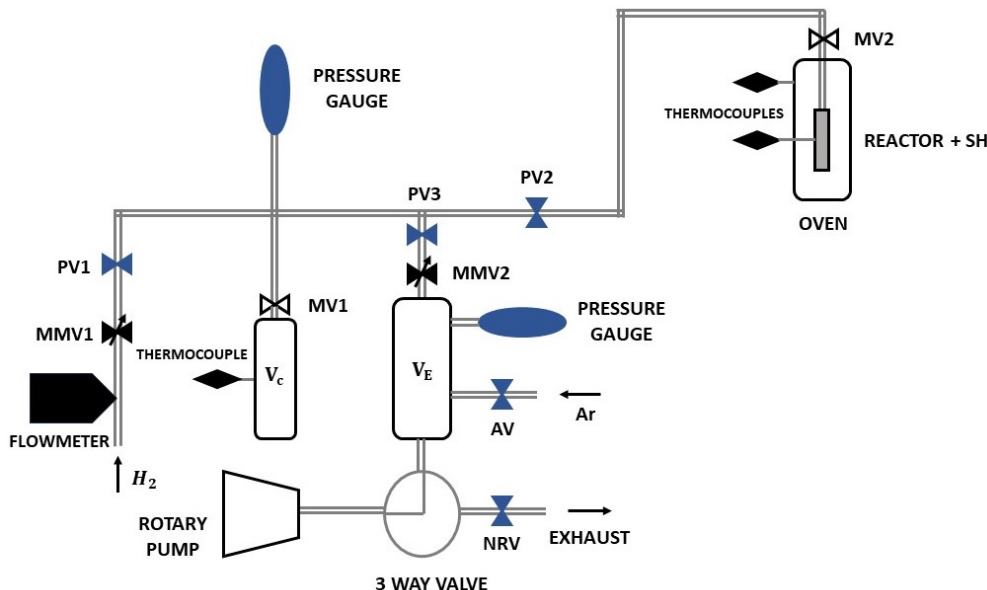
Figure 2.1: Schematics of the apparatus deployed during the experiments. It is based on Sievert's geometry to perform volumetric measurements. Each section of the setup is connected to the others through pneumatic valves (PV), manual valves (MV) and micrometric valves (MMV). The pressure is measured by the main pressure gauge, while the temperature is controlled by three thermocouples.

and the pressure gauge sensitivity are the determining factors in establishing the minimum mass of hydrogen measurable in the apparatus.

2.1.2 Flow meter, thermocouples, pressure gauges

The flow meter (El-Flow by Bronkhorst) is designed to operate in a pressure range of $100 \, mbar - 400 \, bar$, specifically with molecular H_2. It is coupled with a micrometric valve that determines the total flow of hydrogen introduced in the apparatus.

The thermocouples, type K, operate in a range of $-200°C$ to $1200°C$ and are connected to the reactor walls, the oven and the external surface of the calibrated volume, with a sensitivity of $\pm1°C$ for the formers and $\pm0.1°C$ for the latter. The evaluation of hydrogen moles strongly relies on these temperature values since they are directly plugged into the perfect gas equation.
It is noteworthy to observe that, due to a temperature gradient between the reactor walls and the oven, a difference in the temperature reading will always exist.

There are two pressure gauges (MKS 722A Baratron capacitive manometers) in the system, one directly connected to the apparatus pipelines and the other

connected to the expansion volume. The former operates in a $0 - 20\ bar$ range, with a 0.5% sensitivity on the reading. By opening or closing the pneumatic valve PV2 and the manual valve MV2, it is possible to establish the pressure value inside the V_{cx}, V_{cxt} and the total volume of the apparatus. Therefore, the pressure sensor is crucial in the uncertainty associated with the hydrogen moles evaluation. Since the experiment should be carried out in a controlled environment, a thermal insulating foam plastic coat has been deployed to cover the pressure sensor.

2.1.3 Pneumatic and Manual valves

The micrometric valves are used to regulate the input and output hydrogen flow. The MMV1 input valve should always be kept to its minimum opening, guaranteeing a well-controlled gas flow. The same condition should be applied to the MMV2 to avoid overshooting and undershooting in the pressure regulation procedure. The pneumatic valves PV1, PV2 and PV3, controlled by the software by means of solenoid valves operating with 6 bar of air, regulate the gas flow in the entire apparatus. They identify different regions of the setup with volumes V_{cx} (PV2 closed, MV1 opened) and V_{cxt} (PV2 opened, MV2 closed), as indicated in Figure 2.4. The PV1 controls the hydrogen input, while the PV3 manage the gas output. The PV2 valve is of fundamental importance to perform the kinetic and PCI measurements, dividing the pre-chamber volume V_{cx} from the rest of the setup. The dead volumes occupied by the inner pistons are associated with a variation in the apparatus pressure of $2\ mbar$, a value compatible with the uncertainty of the pressure measurement.
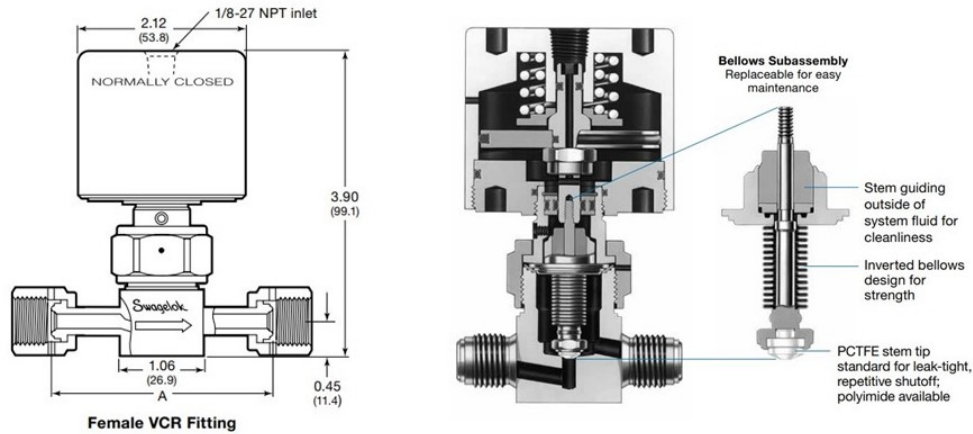
Figure 2.2: Cross section of the pneumatic valve from Swagelok deployed in the apparatus [26].

Figure 2.3: Swagelok components of the reactor chamber. From the left: Gland, Female Nut, filtered Gasket, Body, Gasket, Female Cap [26].

2.1.4 The oven and the reactor

The cylindrical oven has a resistor surrounding the inner core and a thermal insulator as a coating. A thermocouple regulates the oven temperature through an electric regulator. The maximum range of the resistor is 500 °C. The reactor is constituted of several stainless steel sections (Figure 2.3) capable of high-temperature and pressure operations. A silver thread improves element lubricity, avoiding gas leaks. Leaks are also prevented by inserting a thin silver ring (gasket) between the body and the female cap. This object acts as a vacuum seal due to its deformation when the reactor is closed and should be substituted every time this is opened. The gasket at the reactor entrance is provided with a filter, avoiding powder spreads inside the apparatus. The sample holder (SH) is a stainless steel cylinder hosting the powder and allowing hydrogen to flow in and out. The whole structure is connected to the rest of the setup through the manual valve MV2 to a capillary pipe, thus avoiding temperature gradients between the oven and the apparatus and unused passive volume sections.

2.1.5 The expansion volume

The expansion volume operates to evacuate the system. It is connected to the rotary pump, thus working in a dynamic vacuum. When the exhausting procedure is activated (to reduce hydrogen pressure inside the system), the connection between the expansion volume and the rotary pump is interrupted by means of a three-way valve. Hydrogen from the apparatus enters the expansion volume and is mixed with argon, then ejected by the non-return valve (or the rotary pump if the pressure is below 1 bar). Then, the vacuum is performed once again in the volume.
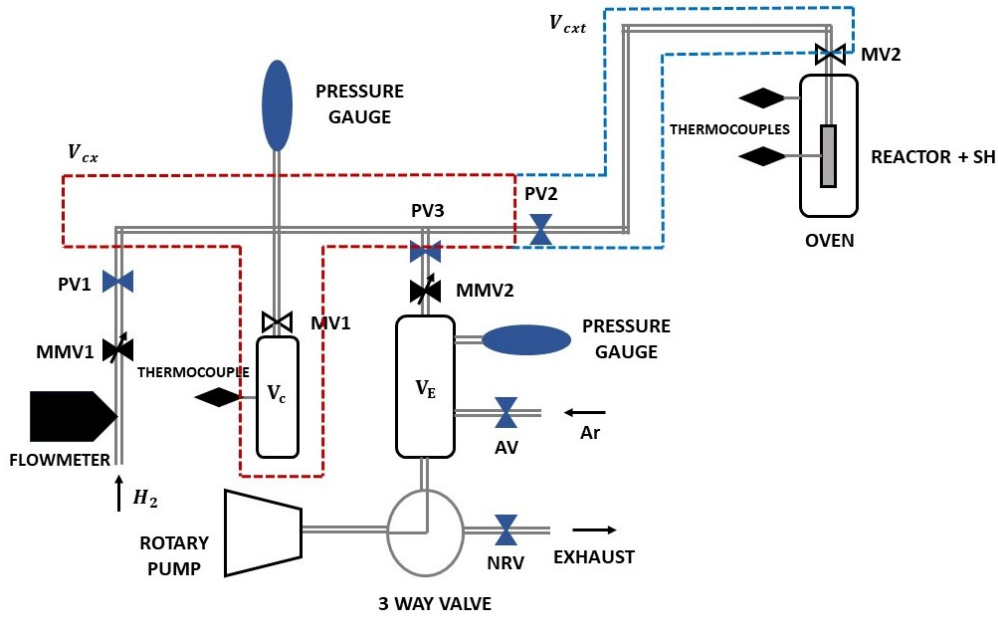
Figure 2.4: The same Sievert's apparatus reported in the previous section is shown with clear segregation of the two main compartments of the setup V_{cx} and V_{cxt}. The latter is obtained by opening the PV2, allowing hydrogen to flow up to MV2.

2.2 Sievert's measurements

This section describes the procedure followed to carry out *PCIs* and *kinetic* measurements, along with considerations on the uncertainty and systematic error corrections.

2.2.1 *PCIs* and wt% evaluation

This section describes the procedure to estimate the total gravimetric density of absorbed or desorbed hydrogen. The calculations are based on the application of the perfect gas equation, which is assumed to be valid in the operating pressure range (the ideal gas law should be corrected with the Van der Waals equation for pressure higher than 50 *bar* [15]).

A Pressure-Composition-Isotherm (PCI) curve is obtained by carrying out a series of small kinetics on the sample near the equilibrium pressure to establish the amount of hydrogen absorbed or desorbed. In case of an absorption measurement, for instance, the pressure in the V_{cx} volume is increased (starting from 0 bar), stabilised, and recorded by the sensor, and then the PV2 is opened, allowing hydrogen to flow in the reactor. The final pressure is recorded, and the process

can move on. Thus, at the kth step, the section of the apparatus going from the PV2 (closed) to the reactor will be at the pressure p^{k-1}, while the pressure in the V_{cx} volume can be set to p_{cx}^k.

At equilibrium, the number of moles in the system will depend on the pressure set in the V_{cx} and the pressure p^{k-1}:

$$n_i^k = \frac{p_{cx}^k V_{cx}}{RT_{cx}} + \frac{p_{cxt}^{k-1}\left(V_{cxt} - V_{cx}\right)}{RT_{cxt}} + \frac{p_{cxt}^{k-1}\left(V_{sh} - \frac{M_{sample}}{\rho_{sample}}\right)}{RT_{sh}}, \qquad (2.1)$$

while the final number of moles after the PV2 opening will be:

$$n_f^k = \frac{p_{system}^k V_{cxt}}{RT_{cxt}} + \frac{p_{system}^k\left(V_{sh} - \frac{M_{sample}}{\rho_{sample}}\right)}{RT_{sh}}, \qquad (2.2)$$

where $R = 83.14\ bar\ cm^3\ mol^{-1}\ K^{-1}$ is the perfect gas constant, ρ_{sample} is the sample density along with its mass M_{sample}, T_{cx} and T_{cxt} are the temperatures of the sections exposed to ambient T, T_{sh} is the temperature in the reactor.

Note that p_{system}^k is the final pressure reached by the apparatus when the PV2 is opened. Therefore, the possible variation in the number of moles given by hydrogen absorption/desorption will be equal to:

$$\Delta n^k = n_i^k - n_f^k \qquad (2.3)$$

By summing over the whole process, the total number of moles is identified:

$$\Delta n_T = \sum_{k=1}^{N} \Delta n^k \qquad (2.4)$$

The overall hydrogen concentration c_H (expressed in $wt\%$) at the end of the process will be equal to:

$$c_H = \frac{\Delta n_T M_{H_2}}{M_{sample}} \times 100 \qquad (2.5)$$

where $M_{H_2} = 2.016 g/mol$ is the hydrogen molar mass and M_{sample} is the powder mass inside the sample holder.

Furthermore, since each Δn^k corresponds to a variation at each step, it is possible to calculate the single-step concentration c_H^k and plot it versus the final pressure p_{system}^k, providing the so-called Pressure-Composition-Isotherm (PCI) curve.

2.2.2   The wt% uncertainty

Several factors may contribute to the uncertainty associated with gravimetric density calculations:

- gas purity: CO_2, H_2O, O_2 may oxidize the sample inhibiting its absorption properties. For this reason, the hydrogen line is directly connected to high-purity (99.99%H_2) gas.

- line leaks: pressure variations that are not consistent with hydrogen sorption, such as apparatus leaks, could be mistaken for hydride formation as well, jeopardising the accuracy of the measurements.

- temperature fluctuations, dead volumes: the number of sorbed moles relies on the ideal gas law, which depends on accurate temperature and pressure values. Even slight variations could compromise the measures. Dead volumes associated with closed valves don't represent an issue in this pressure range since they contribute to an increase of 2 $mbar$ in the pressure sensor reading, a value compatible with gauge uncertainty.

- uncertainty on the sample mass: depending on the scale used for the powder preparation.

Nevertheless, the main contributions are given by the gauge pressure uncertainty, by construction equal to the 0.5 % of the reading, the error on the apparatus volumes, meticulously calibrated before starting the main experiments and temperature fluctuations.

As stated in the previous sections, measurement accuracy strongly relies on the overall volume deployed in the apparatus: a more accurate analysis relies on a smaller setup volume, provided that the sample has a mass of some tens of mg. In the *kinetic* process, it is reasonable to keep the valve connecting the external calibrated volume opened, thus providing a higher amount of hydrogen moles and allowing the sample to completely absorb hydrogen before reaching the plateau pressure. Instead, it is suggested to exclude the V_c volume when performing a PCI, reducing the total number of moles at the same pressure and increasing the sensitivity on the measurements.

Therefore, when considering pressure accuracy, the minimum change in the hydrogen mass detectable on the apparatus volume is around $50\mu g$, corresponding to a $0.01wt\%$ uncertainty on the gravimetric density provided a sample of 500 mg. Since the pressure gauge accuracy is 0.5 % of the reading, affecting both (2.6) and (2.7), when comparing the number of moles (computed through (2.3)) calculated considering a certain pressure and the number of moles obtained when integrating

the uncertainty on that pressure value, a value of $50\mu g$ hydrogen emerges.

By propagating the uncertainties associated with volume and temperature in eq. (2.5), the final uncertainty of $0.08wt\%$ can be established for a 500 mg sample.

2.2.3 Further corrections

By considering Figure 2.4 it is reasonable to assume that the hydrogen moles calculations could benefit from a volume correction: a section of the apparatus starting from the MV2 and ending on the edge of the oven that is accounted in the sample holder volume V_{sh} is not exposed to the oven temperature, thus providing a different number of moles in the final calculations. For this reason, eq. (2.1) and (2.2) have been corrected as follows:

$$n_i^k = \frac{p_{cx}^k V_{cx}}{RT_{cx}} + \frac{p_{cxt}^{k-1}\left(V_{cxt} - V_{cx} + V_{corr}\right)}{RT_{cxt}} + \frac{p_{cxt}^{k-1}\left(V_{sh} - \frac{M_{sample}}{\rho_{sample}} - V_{corr}\right)}{RT_{sh}}, \quad (2.6)$$

$$n_f^k = \frac{p_{system}^k\left(V_{cxt} + V_{corr}\right)}{RT_{cxt}} + \frac{p_{system}^k\left(V_{sh} - \frac{M_{sample}}{\rho_{sample}} - V_{corr}\right)}{RT_{sh}}. \quad (2.7)$$

In addition, the corrected volume predicted by the model is compatible with the empirical evaluation of the section at different temperatures, resulting in a predictive model of the possible virtual leaks when spanning a wide temperature range.

Another possible correction would involve real gas behaviour (typically neglected below 50 bar [15]), following Van der Waal's equation:

$$\left(p + \frac{an^2}{V^2}\right)\left(V - nb\right) = nRT, \quad (2.8)$$

where p, V and T are the pressure, volume and temperature of the gas, $R = 8.314J\ K^{-1}\ mol^{-1}$ is the perfect gas constant, $a = 0.2476L^2\ bar\ mol^{-2}$ is the molecular interaction parameter and $b = 0.02661L\ mol^{-1}$ is the co-volume of the hydrogen molecules. By deploying eq. (2.8) to calculate the number of moles in the system, a difference of 0.06 $wt\%$ has been found, compatible with the uncertainty on the gravimetric density.

2.2.4 *Kinetics*

Kinetic measurements have been carried out by keeping the ratio $pressure(t)/p_{eq}$ as constant as possible. The reason behind this choice lies in the physics of the

process: hydrogenation and de-hydrogenation of metal should be carried out in isobaric conditions (and at fixed temperature), avoiding the introduction of an external driving force gradient that would completely change the kinetic of the event. Furthermore, suppose the instantaneous pressure of the gas is too close to the equilibrium pressure. In that case, it is impossible to establish if the process has slowed down because of complete hydrogenation or de-hydrogenation of the metal or simply because the driving force is insufficient to induce absorption/desorption.

The pressure-time profile of the analysed samples can be fitted with an exponential function of the form

$$p(t) = e^{-(k(t-t_0))^n} + c \tag{2.9}$$

in the case of absorption, and

$$p(t) = 1 - e^{-(k(t-t_0))^n} + c \tag{2.10}$$

in the case of hydrogen desorption, which resembles the JMAK model in its exponential form.

Then, in order to apply the model to the gathered data in linear form, it was necessary to evaluate the reaction fraction ξ, following the relation:

$$\xi = \frac{p_i - p(t)}{p_i - p_f}. \tag{2.11}$$

The rate constant k and the Avrami exponent n obtained from eq. (1.27) should be consistent with the ones extracted from eq. (2.9) and (2.10) where the same JMAK model is applied with a different algorithm and fitting window.

Figure 2.5 shows the possible Arrhenius trend in the ideal case (blue dots) and when an external driving force affects the model. Indeed, if the p/p_{eq} ratio increases significantly with decreasing temperature (orange dots), the fictitious driving force will result in a larger value of the rate constant k, thus jeopardizing the expected value of the activation energy E_A that can be extracted from the plot. On the contrary, if the ratio decreases (yellow dots), a smoother trend is expected in the pressure vs time profile, caused by a lower rate constant that would bring higher activation energy for the process.

2.3 Structural, morphological and elemental characterisation

2.3.1 X-Rays Powder Diffraction (XRD)

The crystalline structure and phase characterisation have been carried out with an X'Pert Pro PANalytical X-ray diffractometer, Bragg-Brentano geometry, Cu
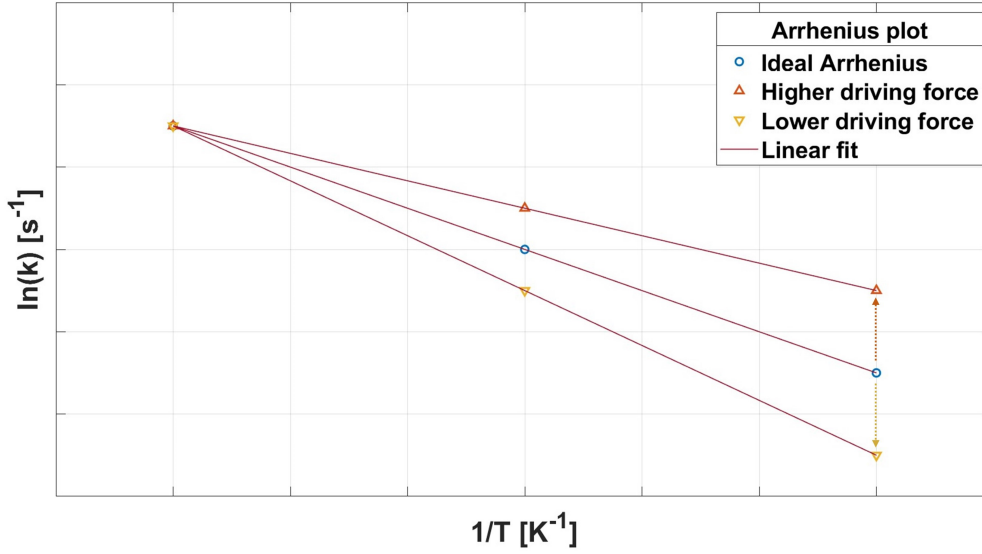
Figure 2.5: Simulation of three different scenarios for the Arrhenius plot: blue dots represent the ideal case where the p/p_{eq} ratio is kept constant when varying the temperature T, orange dots represent the case of increasing ratio with decreasing T and yellow dots represent the case of decreasing ratio with decreasing T. Therefore, $|E_A^{higher\ ratio}| < |E_A^{ideal}| < |E_A^{lower\ ratio}|$.

Kα source, energy $E = 8.04 keV$, $\lambda = 1.5406$ Å with Ni and Cu filters, $1/2°$ slits. All diffractograms have been analysed through Rietveld's refinement method. The refinement has been enriched with the March-Dollase degrees of freedom to account for possible preferential orientation. This algorithm accounts for non-random plane distribution (that typically generates anisotropic effects in peak intensity) through a convolution of the Orientation Distribution Function (ODF) with the calculated diffraction pattern. Data have been visualised by deploying the High Score Plus software [27] and analysed through MAUD software [28]. 3D crystallographic rendering was possible thanks to VESTA [29].

2.3.2 Scanning Electron Microscopy (SEM)

The morphological and elemental analysis has been instead carried out through a Leica Cambridge Stereoscan 360 SEM, tungsten filament, Everhart Thornely secondary and backscattered electrons detector, Oxford Instrument 7060 EDX detector with an energy resolution of $133\,eV$ at $5.9\,keV$. The micro-analysis software deployed is an INCA Oxford Instrument. Sample morphology has been characterised through secondary-electron analysis, while elemental and compositional maps have been carried out through energy-dispersive X-ray spectroscopy.

2.4 Materials

2.4.1 Pd

The kinetic measurements were carried out with $m = 0.198 \pm 0.001\ g$ of 99.97% pure Pd, density of 12.02 $g\,cm^{-3}$, grain size 56 μm, from Koch chemicals Itd. A significant amount ($m = 0.998 \pm 0.001\ g$) was deployed for PCI measurements. The difference in the sample mass during the experiments is justified by the limit set by the pressure sensor range that inevitably affected the p/p_{eq} ratio along absorption/desorption cycles: indeed, it is possible to establish the pressure drop due to hydrogen intake/release, thus estimating the final pressure that the system will reach, to be compared with the equilibrium pressure especially when the former is below 1 bar (DES) or above 15 bar (ABS).

The V_c section was connected to the rest of the apparatus through the opened PV2 to guarantee the proper amount of hydrogen to be absorbed by the sample.

2.4.2 LaNi$_5$

The kinetic and PCI measurements were carried out with $m = 0.493 \pm 0.001\ g$ flakes of 99.9 % pure $LaNi_5$ from Alfa Aesar, density of 7.95 $g\,cm^{-3}$ and nominal gravimetric density of 1.5 $wt\%$.

The V_c section was connected to the rest of the apparatus through the opened PV2 to guarantee the proper amount of hydrogen to be absorbed by the sample.

2.4.3 Hydralloy C5

The kinetic and PCI measurements were carried out with $m = 0.544 \pm 0.001g$ flakes of TiZrMnVFe from AMG titanium alloys&coatings, $2 - 10\ mm$ grain size, density of 6.40 $g\,cm^{-3}$ and nominal gravimetric density of 1.8 $wt\%$.

The V_c section was connected to the rest of the apparatus through the opened PV2 to guarantee the proper amount of hydrogen to be absorbed by the sample.

2.4.4 TiFe$_{0.9}$Ni$_{0.1}$

The activation and PCI measurements were carried out with $m = 0.479 \pm 0.001\ g$ of crushed TiFe$_{0.9}$Ni$_{0.1}$ arc melted at the Chemistry Department of the University of Turin, with a density of 6.79 $g\,cm^{-3}$, expected gravimetric density equal to 1.1 $wt\%$ for the mono-hydride. The V_c section was connected to the rest of the apparatus through the opened PV2 to guarantee the proper amount of hydrogen to be absorbed by the sample.

2.4.5 Ball Milling

The milling procedure was carried out by introducing 2 g of TiFe produced by GoodFellow (dry powder, 150 μm grain size) in a Spex CertiPrep 8000 Mixer/Mill. The whole experiment was performed under air, standard pressure environment. Both pot and balls were made of hardened steel, in a ratio of balls-to-powder mass equal to 2:1. The milling time spanned in a large interval going from 10 minutes to 24 hours. Another attempt was made with a different sample composed of elemental Ti and Fe to form 8 g of TiFe in the proper stoichiometric ratio. The balls-to-powder mass ratio was 2:1, probing after 2 and 24 hours. The latter experiment was carried out in Ar inert atmosphere.

2.4.6 Arc melting

The $TiFe_{0.9}Ni_{0.1}$ sample was prepared with an Edmund Bühler D-7400 Tübingen arc melter, water-cooled copper crucible plate, titanium electrode with a maximum temperature of $3500\,°C$. The elemental metals were mixed starting from 50% Ti, 45% Fe and 5% Ni rods.
Pre-alloying was not necessary since all elements show similar fusion temperatures. The chamber was pre-treated with Ar cycles, reaching the final pressure of $10^{-6}\,mbar$.
A Ti getter triggered each melting cycle (4 cycles in total), with a maximum current of $450\,A$ and an average current of $300\,A$.

The procedure was carried out in collaboration with the Chemistry department of the University of Turin.

2.5 Sample *activation*

When dealing with activation, there are three main alternatives: a pressure swipe with constant temperature, a temperature swipe with constant pressure or a combination of the two. The general idea is to span in a pressure range compatible with absorption and desorption processes to enhance alloy cracking and hydrogen diffusion while spanning in a wide temperature range to induce a structural redistribution of the atoms, thus promoting a fresh surface ready for chemisorption.

2.5.1 $LaNi_5$ activation

Several cycles of absorption and desorption were performed for the $LaNi_5$ samples. In particular:

- The first sample (in the form of powder) was annealed at 200 °C with eight cycles of 20 *bar* and vacuum of hydrogen, each lasting 20 min.

- The second sample (as received, in the form of flakes) was prepared in an inert (N_2) atmosphere. Since the hydriding properties of the material were not positively affected by this procedure, the flakes were activated following the previous technique.

- A third sample was annealed at 100 °C and then cycled with hydrogen, demonstrating that $LaNi_5$ merely requires mild conditions to be activated.

2.5.2 *Hydralloy C5* activation

For what concerns the Hydralloy C5 sample, the following protocol was adopted:

- 1 h at $T = 100$ °C and 1 h at $T = 250$ °C with cycles of high pressure (19 *bar*) and vacuum resulted in partial sample activation.

- A second sample was annealed up to $T = 155$ °C, then 2 cycles of high-pressure absorption and 2 of vacuum desorptions were carried out.

- Temperature was then brought down to $T = 8$ °C while keeping $p = 19.5$ *bar*.

2.5.3 *$TiFe_{0.9}Ni_{01}$* activation

Regarding $TiFe_{0.9}Ni_{01}$ activation, it was necessary to overcome the sensor limit in order to induce the sample activation:

- Crushed powder was annealed for 5 h at $T = 340$ °C, high pressure at 40 *bar* (the high pressure was reached by introducing 20 *bar* at room T, then increasing the temperature up to the final value of annealing by isolating the reactor from the apparatus through the manual valve MV2).

- The procedure seemed to be insufficient for the sample to absorb hydrogen, therefore a second annealing was performed for 2 h and 30' at $T = 420$ °C, expected pressure in the reactor equal to $p = 45$ *bar*.

- Finally, after four cycles of high pressure (20 *bar*) and vacuum (15' each) at $T = 50$ °C, the sample seemed to be activated for hydrogen absorption.

Chapter 3

Analysis and results

In the following chapter, the results of the performed experiments are reported. As a preliminary test, a calibration procedure has been carried out to establish the volume of the apparatus, thus its response in the ideal gas law limit, along with the uncertainty on the $wt\%$ measurements. Furthermore, each alloy has been characterized with SEM analysis, providing a morphological and compositional map and a powder XRD profile to obtain information on the phase and the crystal structure.

3.1 Calibration measurements and pVT map

3.1.1 Volume determination

The calibrated reservoir volume has been measured by filling it with distilled water from a graduated cylinder, yielding a value of $V_c = 51.2 \pm 0.1 \ cm^3$. The other partial volume calibration was performed by introducing hydrogen each time with a different pressure inside the calibrated volume, then opening one valve at a time, measuring the pressure at each step. The uncertainty of the measurements depends on the pressure error and temperature fluctuations. Table 3.1 shows the average values along with their uncertainties:

3.1.2 Background calibration and pVT map

Figure 3.1 shows the time profile of a background calibration performed at 119 °C, simulating an absorption ramp-PCI measurement. The red dots identify the pressure in the V_{cx} section before opening the PV2 valve. They are referred to as p_{cx} in

	Volume $[cm^3]$	Error $[cm^3]$
V_c	51.2	0.1
V_{cx}	65.7	0.5
V_{cxt}	71.7	0.5
V_{sh}	5.90	0.05
V_T	77.6	0.5

Table 3.1: Calibration measurements: section volumes averaged over 3 initial pressure conditions (1, 5, 10 bar).

this context and will be called *p1* points from now on. The yellow dots represent the pressure values in the system once the PV2 has been opened. They are referred to as p_{system} and will be called *p2* points henceforth. To understand the procedure adopted during these ramps, the reader can refer to Appendix A, where a detailed description of the relation between the pressure values and the PV2 valve status is reported.

In the absence of a sample that can absorb or release hydrogen, the system is supposed to behave following the ideal gas law without any loss or increment in the number of moles. Its response has been characterised as shown in figure 3.1 for different temperature values. The results are shown in figure 3.2, which demonstrates the ideal gas law validity in the low-temperature limit (below 120 °C).

Figure 3.2-A shows the dependence of each p2 pressure value on the initial p1 condition at different temperatures. A linear behaviour is expected, confirmed by the fitting model applied to the collected data.

Figure 3.2-B shows the discrepancy between the expected value of pressure after opening the PV2 (computed with the ideal gas equation) and the collected data at each step (each step corresponding to a pressure increment in the V_{cx} section of 1 *bar*).

Table 3.2 shows the increasing discrepancy with increasing temperature. It is noteworthy to underline that the pressure reached by the apparatus is always greater than the expected value, presumably due to the presence of a reactor section exposed to room temperature that introduces a systematic error when the temperature in the oven is increased. This non-linear behaviour has been accounted for, and the systematic error has been corrected by adding an additional term in the mole evaluation accounting for this fictitious volume. The correction is based on several volume-vs-temperature values interpolation to adjust for this systematic error (see section 2.2.3).
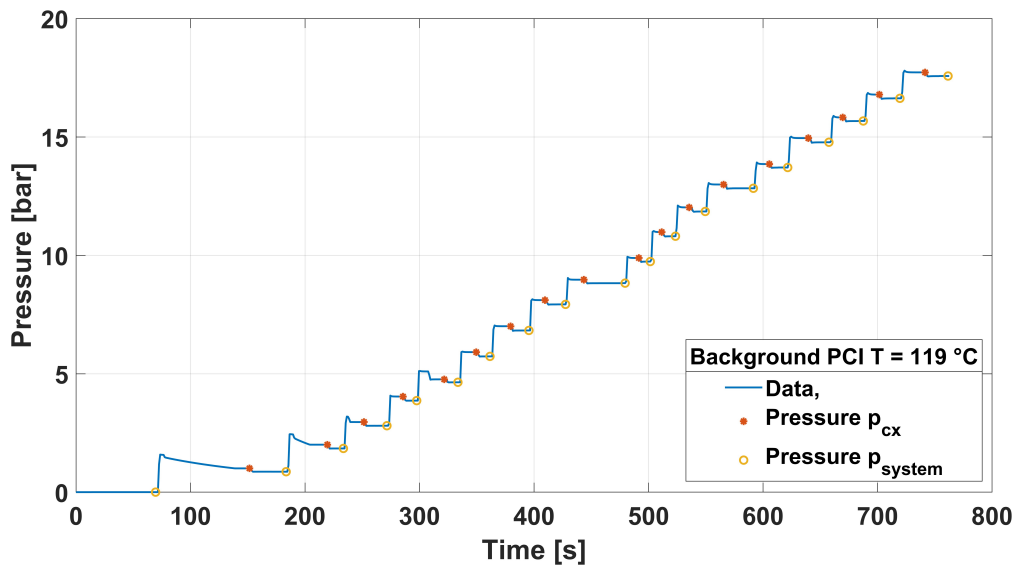
Figure 3.1: Background measurement for PCI evaluation, empty sample holder, $T = 119\,°C$. The pressure increment is roughly $1\,bar$, with the red dots p_{cx} being the pressure in the V_{cx} section, named p1, and the yellow dots p_{system} being the pressure after opening the PV2, named p2.
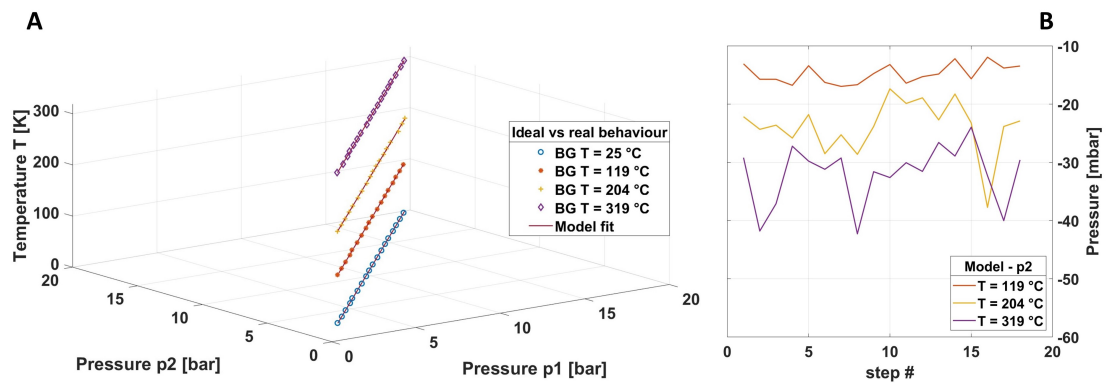
*Figure 3.2: PCI background calibration for $T = 25, 119, 204$ and $319\,°C$. **A)** p2 vs p1 at different temperatures. Data have been fitted with the ideal gas model. **B)** Difference between the expected value of pressure computed with the ideal gas law and the collected data for different temperature values. The discrepancies are reported in table 3.2.*

T [$°C$]	Δp [mbar]
119	14.8 ± 0.1
204	23.8 ± 0.1
319	31.9 ± 0.2

Table 3.2: $|p^{comp} - p^{exp}|$ increasing with increasing temperature. The experimental value is always greater than the computed one.

3.2 Pd characterisation

3.2.1 Kinetics

Figure 3.3 shows the absorption and desorption profile in terms of concentration vs time of palladium powder. As expected, the material was readily inclined to absorb hydrogen, showing fast kinetics for each measurement. The ratio p/p_{eq} was kept constant during each cycle and when varying the temperature (in the limit of the apparatus), with a value of 1:3.6 at $T = 146$ °C, 1:3.7 at $T = 196$ °C and 1:3.9 at $T = 250$ °C in the desorption measurements. It is noteworthy to observe that higher temperatures result in steeper p vs t profiles, as expected for a thermally activated process. The time scales of the palladium kinetics are compatible with the pressure-balancing processes of the apparatus, resulting in a jeopardized measure of the rate constant. Unfortunately, it was not feasible to keep the pressure ratio constant in the absorption process with the chosen temperature range due to the limit set by the sensor range, thus jeopardizing the expected trend when increasing temperature. Indeed, the ratio p/p_{eq} is higher at lower temperatures, resulting in a higher rate constant, in contrast with the expected Arrhenius profile (blue dots in absorption section, figure 3.3).

The reversible gravimetric density at 146 °C is 0.60 ± 0.08 $wt\%$, in agreement with literature [30] [31]. The absorption/desorption profiles are rather symmetric even at high temperatures, with lower maximum gravimetric density at higher T, in agreement with the thermodynamic PCIs results.

3.2.2 PCIs and Van't Hoff plot

Figure 3.4 shows the PCIs for the $Pd - H_x$ system (A) along with the Van't Hoff plot computed on the mean value of the absorption pressure, desorption pressure and the geometric mean of the two (B). The uncertainties on the former values were estimated as the maximum errors of the chosen interval, while the uncertainty on the latter was estimated with error propagation. The reversible gravimetric density is 0.56 ± 0.08 $wt\%$, in good agreement with the results of [31] and the previous
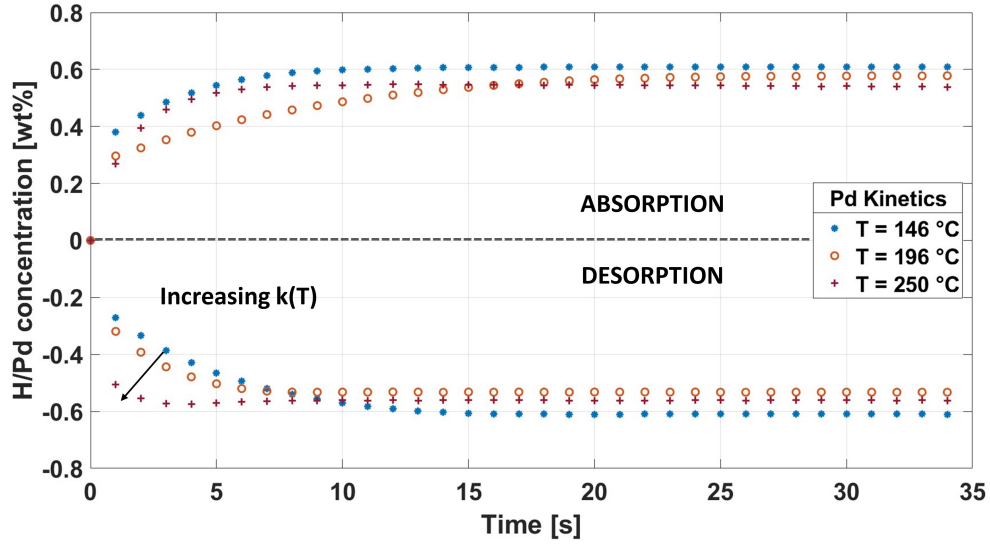
Figure 3.3: Concentration vs time profile for Pd sample at different temperatures. The desorption pressure ratio was kept constant at 1:3.8 when varying T, thus reflecting the expected Arrhenius behaviour of increasing rate constant k(T) with increasing T. The maximum gravimetric density is 0.60 ± 0.08 wt%. The pressures in the middle of the desorption process were $[0.25, 0.8, 1.9]$ bar with respect to the equilibrium pressure $[0.9, 3, 7.5]$ bar respectively at the temperature $[25, 49, 69]$ °C.
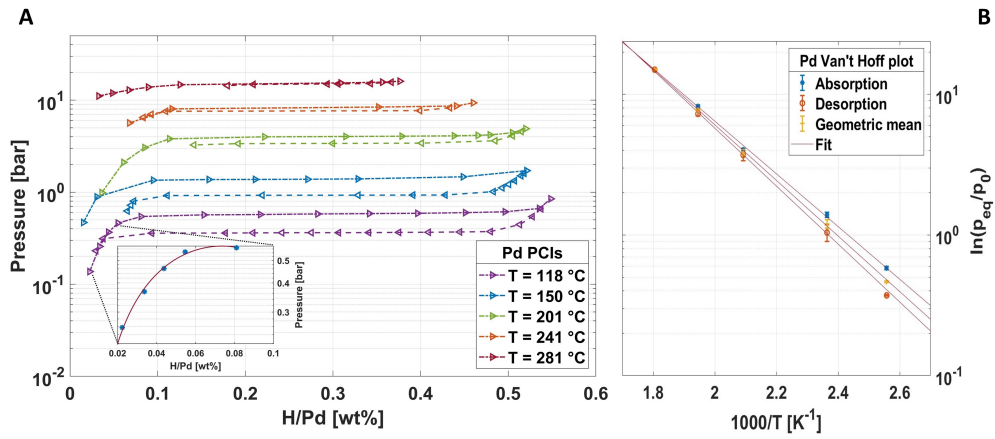
*Figure 3.4: **A)** PCIs for Pd powder in the temperature range $118 - 281$°C. The gravimetric density is 0.56 ± 0.08 wt%, in good agreement with [30] [31]. The presence of hysteresis in plateau pressures is justified in section 1.2.3. **B)** Van't Hoff plot of the averaged plateau pressures at different temperatures. The resulting thermodynamic parameters are reported in table 3.3*

	$\Delta H^{exp}[kJ\,mol^{-1}]$	$\Delta S^{exp}[J\,mol^{-1}\,K^{-1}]$	$\Delta H^{ref}[kJ\,mol^{-1}]$	$\Delta S^{ref}[J\,mol^{-1}\,K^{-1}]$
$\alpha \to \beta$	-35.8 ± 0.6	-87 ± 1	-37.4 ± 0.3	-92.5 ± 0.8
$\beta \to \alpha$	39.5 ± 0.6	93 ± 1	39.0 ± 0.5	92.5 ± 1.3
MEAN	37.8 ± 0.6	90 ± 1		

Table 3.3: Pd Van't Hoff model parameters extracted by fitting the logarithm of the averaged plateau pressures at each temperature following eq. (1.14). The first two columns show experimental results with statistical uncertainties, while the last two list reference data by [31].

measurements. The enthalpy and entropy of formation associated with the three Van't Hoff plots are shown in table 3.3 along with the results of [31].

As expected, hysteresis between the absorption and desorption plateau pressure exists due to different kinetic mechanisms related to hydrogen diffusion, along with the presence of stress at the $\alpha - \beta$ coherent interface that produces a thermodynamic energy barrier that changes the value of the chemical potential, as reported in section 1.2.3. It is noteworthy to observe Sievert's behaviour of the PCIs for low H concentration, with a quadratic pressure vs c_H profile.

3.3   LaNi$_5$ characterisation

3.3.1   Structural and morphological characterisation

Figure 3.5 shows the powder diffraction profile of $LaNi_5$ powder in the 2θ range $[25, 90]°$. Data are fitted using Rietveld's refinement analysis, and the results are shown in table 3.4. As visible in the VESTA visualization, the cell is composed of 2 different nickel sites, accounting for 2 and 3 atoms in total, thus confirming the expected stoichiometry.

As reported in table 3.4, lattice parameters are in good agreement with the HighScore Plus results [32]. The residue doesn't show significant misalignment with collected data, confirming the validity of peak shape and position.

Figure 3.6 shows the morphological images collected on $LaNi_5$ powder grains. The elemental analysis is summarised in table 3.5. The average particle size is $10\mu m$.

3.3.2   Kinetics

Soon after sample activation, following the procedure reported in section 2.5.1, it was possible to perform a series of absorption/desorption cycles at different temperatures. Figure 3.7 shows the results of a set of cycles performed on $LaNi_5$
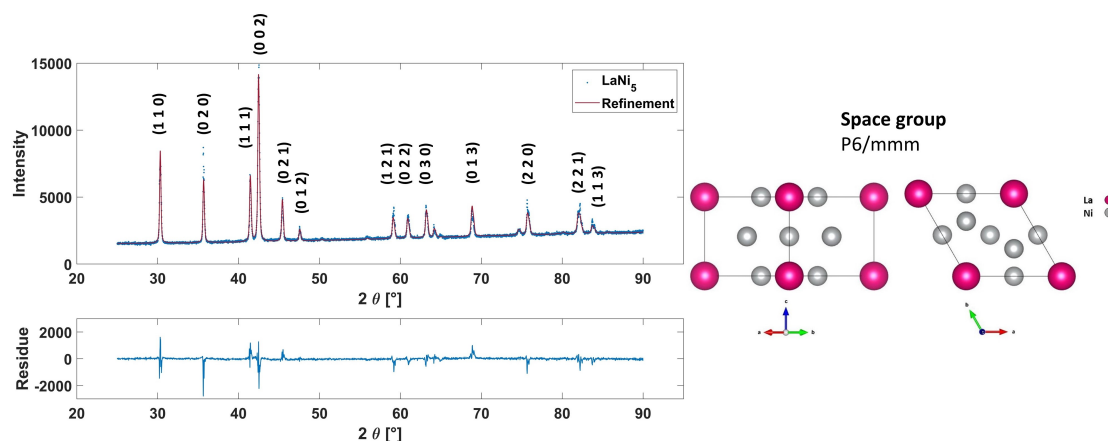
Figure 3.5: XRD powder diffraction profile and Rietveld's refinement analysis of LaNi₅ sample. The residue between collected data and fit is reported at the bottom of the graph. The schematic (generated by VESTA) on the right shows the crystal structure integrated into the refinement, in agreement with reference [32].

	Experimental	Reference
Structure	HCP	HCP
Space group	P6/mmm	P6/mmm
a [Å]	5.0142 ± 0.0002	5.013
c [Å]	3.9820 ± 0.0002	3.984

Table 3.4: $LaNi_5$ Rietveld's refinement lattice parameters compared with HighScore Plus reference [32].
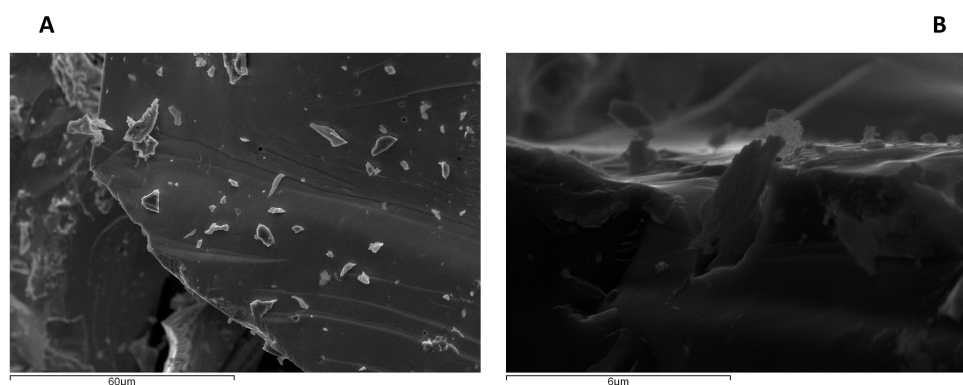
Figure 3.6: $LaNi_5$ SEM morphological analysis.

powder. The temperature ranged in the interval $[25, 49, 69]$ °C due to the pressure

	La	Ni
Nominal [at%]	17	83
Experimental [at%]	17.7 ± 0.5	82.3 ± 0.5

Table 3.5: Nominal and SEM elemental composition for the $LaNi_5$ sample.

limits set by the apparatus and the sample thermodynamics. The maximum gravimetric density reached in these experiments is 1.48 ± 0.08 $wt\%$, in good agreement with [19]. Despite the asymmetry in the two sorption regions, it is possible to appreciate a reduction in the total gravimetric density as temperature increases, as depicted in the next section of PCIs' graphs.
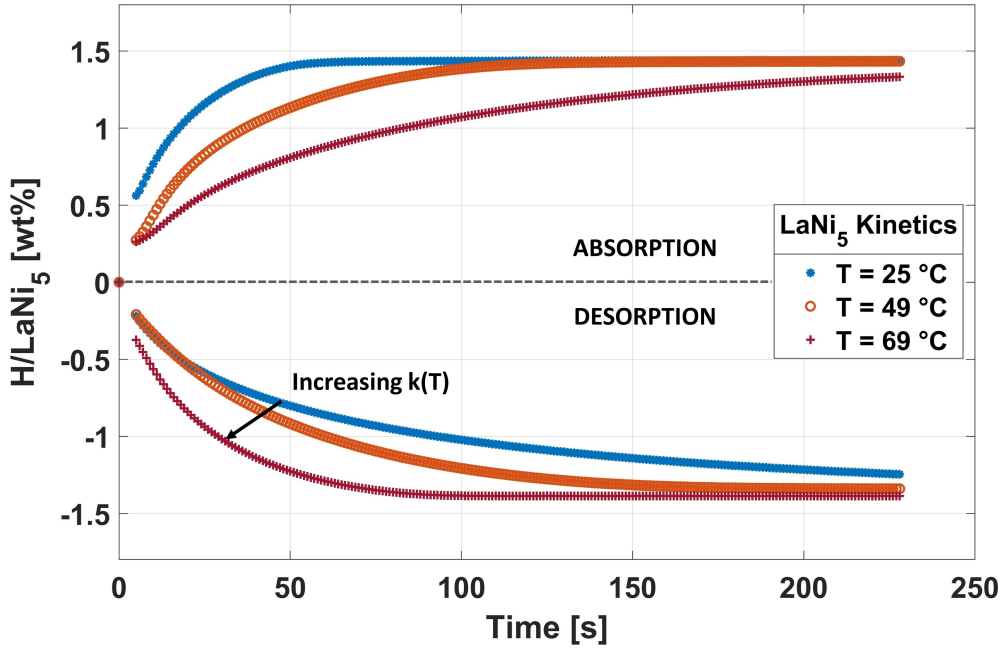
Figure 3.7: Concentration vs time profile for $LaNi_5$ at different temperatures. The desorption pressure ratio p/p_{eq} varied in the range 1:2 to 1:3 when varying T, thus reflecting the expected Arrhenius behaviour of increasing rate constant $k(T)$ with increasing T. The maximum reversible capacity is 1.48 ± 0.08 $wt\%$, in good agreement with the results of [19]. The pressures in the middle of the desorption process were $[1, 2, 3]$ bar to be compared with the equilibrium pressures $[2, 5, 10]$ bar respectively at the temperatures $[25, 49, 69]$ °C.

The absorption profile is affected by an external driving force caused by the gauge's limited range, resulting in a distorted dependence with T that cannot be fitted with the Arrhenius model: the rate constant in the absorption kinetics

decreases with increasing temperature due to the smaller ratio between the starting pressure and the equilibrium pressure set by $LaNi_5$ thermodynamics.

The p/p_{eq} ratio spanned from 1:2 to 1:3 during the desorption measurements, resulting in an increment of the rate constant due to an increment in the external driving force applied on the powder and because of the increasing temperature (following the Arrhenius trend).

Despite the difference of one order of magnitude in $LaNi_5$ kinetics compared with Pd, the concentration-time profile still shows fast absorption/desorption cycles, revealing well-known appealing kinetic properties of this compound.

Figure 3.8 shows the linearization performed on the desorption data at $T = [25, 49, 69]$ °C fitted with the JMAK model following eq. (1.27). The extracted parameters are reported in table 3.6.
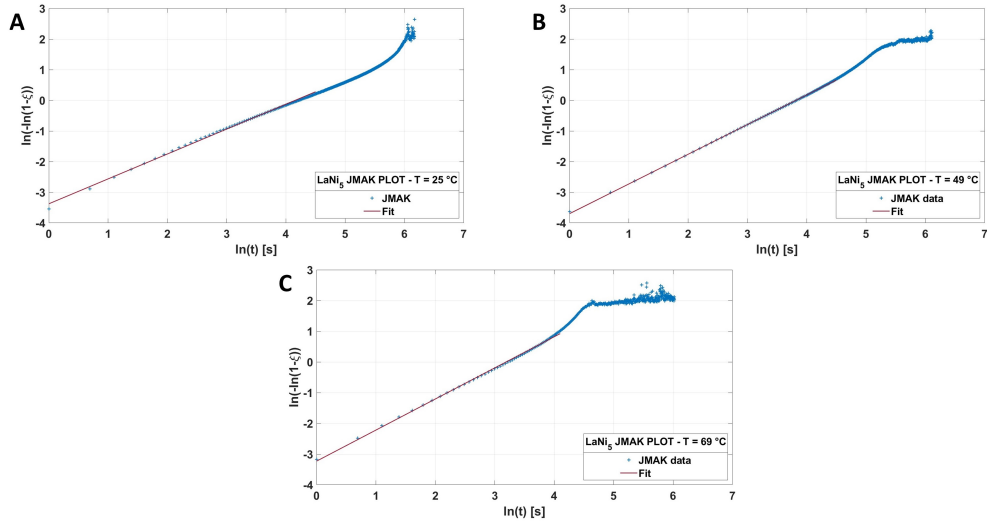
Figure 3.8: JMAK model applied to $LaNi_5$ desorption data at **A)** $T = 25$ °C, **B)** $T = 49$ °C, **C)** $T = 69$ °C.

	25 °C	49 °C	69 °C
k $[ks^{-1}]$	15.32 ± 0.04	22.0 ± 0.1	41.2 ± 0.9
n	0.81 ± 0.01	0.97 ± 0.01	1.01 ± 0.01

Table 3.6: $LaNi_5$ JMAK parameters at different temperatures for desorption data. The rate constant increases with increasing temperature, following the Arrhenius expected trend.

As stated before, the rate constant $k(T)$ increases with increasing temperature, a trend followed by the Avrami exponent, too. Indeed, since $n \in [0.8, 1]$, four
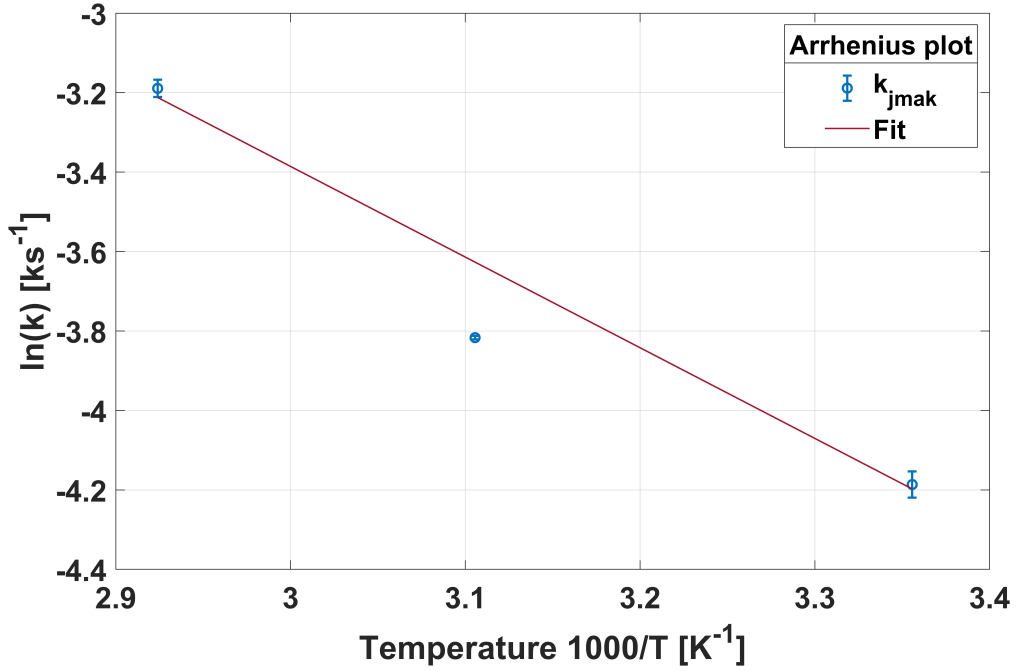
Figure 3.9: *Arrhenius model fitting the $LaNi_5$ desorption kinetic data, $T \in [25, 49, 69] \,°C$.*

possible scenarios may be depicted by following the reasoning exposed in section 1.3.2:

- $[a, b, c] = [0.3, 0.5, 1]$ suggesting a $1 - D$ diffusion-limited process with nucleation rate decreasing in time.

- $[a, b, c] = [0, 0.5, 2]$ in case of $n = 1$, suggesting a $2 - D$ diffusion-limited process with nucleation occurred at the beginning of the event.

- $[a, b, c] = [0, 1, 1]$ in case of $n = 1$, suggesting a $1 - D$ source-limited process with nucleation occurred at the beginning of the event.

- $[a, b, c] = [0.5, 0.5, 1]$ in case of $n = 1$, suggesting a $1 - D$ source-limited process with a decreasing nucleation rate with time.

Therefore, despite the difficulty in interpreting the actual scenario occurring during the desorption kinetic, the most probable event would consist of a $1 - D$ diffusion-controlled process with the nucleation rate decreasing with time.

Figure 3.9 shows the Arrhenius model fitted on the desorption kinetics collected data. The activation energy is found to be $E_A = 19 \pm 2 \; kJ \, mol^{-1} \, H_2$, in good agreement with the results of $E_A^{ref} = 19.7 \; kJ \, mol^{-1} H_2$ obtained by [33]. The

59

$E_A[kJ\,mol^{-1}]$	$k_0[ks^{-1}]$
19 ± 2	32 ± 2

Table 3.7: $LaNi_5$ Arrhenius parameters extracted by the model applied in figure 3.9, in good agreement with the results of $E_A^{ref} = 19.7\,kJ\,mol^{-1}H_2$ obtained by [33].

parameters extracted from the fit are shown in table 3.7. The presence of an external driving force induced by an increasing p/p_{eq} ratio with increasing temperature is reflected in a larger value of the rate constant at high T, slightly increasing the activation energy compared with the theoretical value.

3.3.3 PCIs and Van't Hoff plot

Figure 3.10-A shows the PCIs performed on $LaNi_5$ powders at $T = [28, 49, 69]\,°C$. The observed reversible gravimetric density is $1.39 \pm 0.08\,wt\%$, compatible with the kinetic experiments carried out after activation and the results obtained by [19]. Notably, a hysteresis cycle is observed at each isotherm, suggesting the presence of a thermodynamic energy barrier arising at the coherent metal/hydride interface, resulting in a different value of the chemical potential in hydrogen sorption, as discussed in section 1.2.3.

As expected, the total gravimetric density reduces with increasing temperature, although it was not possible to experimentally determine the critical decomposition temperature T_c.

Figure 3.10-B shows the Van't Hoff equation fitted on the pressure data determined from the mean value of the absorption plateau pressures, desorption plateau pressures and the geometric mean of the two. The uncertainties on the former values were estimated as the maximum errors of the chosen interval, while the uncertainty on the latter was estimated with error propagation. The extracted fit parameters, providing the enthalpy and entropy of formation and decomposition, are reported in table 3.8, which shows good agreement with the literature [19] [34].
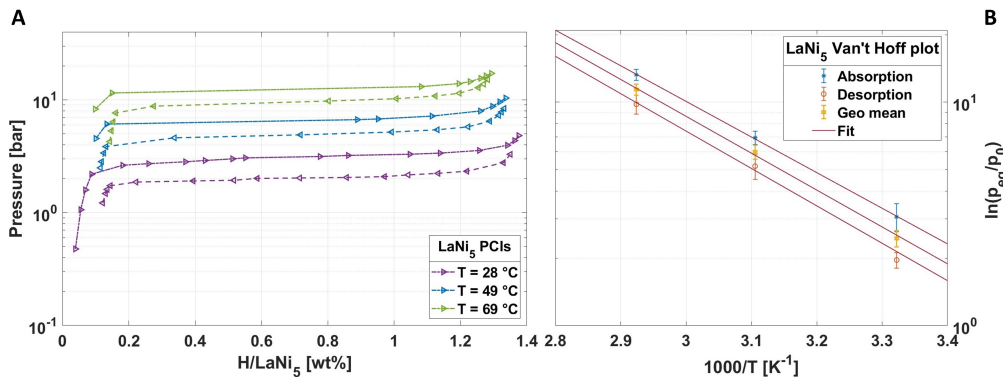
Figure 3.10: **A)***PCIs for LaNi$_5$ powder in the temperature range $28-69$ °C. The gravimetric density is 1.39 ± 0.08 wt%, in good agreement with [19] [34].* **B)** *Van't Hoff plot of the averaged plateau pressures at different temperatures. The resulting thermodynamic parameters are reported in table 3.8.*

	$\Delta H^{exp}[kJ\,mol^{-1}]$	$\Delta S^{exp}[J\,mol^{-1}\,K^{-1}]$	$\Delta H^{ref}[kJ\,mol^{-1}]$	$\Delta S^{ref}[J\,mol^{-1}\,K^{-1}]$
$\alpha \to \beta$	-30.5 ± 0.4	-111 ± 1	-30.4 ± 0.4	-111.5 ± 0.5
$\beta \to \alpha$	32 ± 3	113 ± 8		
MEAN	32 ± 2	113 ± 5		

Table 3.8: LaNi$_5$ Van't Hoff model parameters extracted by fitting the logarithm of the averaged plateau pressures at each temperature following eq. (1.14). The first two columns show experimental results with statistical uncertainties, while the last two exhibit the results obtained by [34].

3.4 Hydralloy C5 characterisation

3.4.1 Structural and morphological characterisation

Figure 3.11 shows the powder diffraction profile of the Hydralloy sample in the 2θ range $[20, 100]$°. Data are fitted using Rietveld's refinement analysis, and the results are shown in table 3.9. As visible in the VESTA visualization, the cell comprises two different sites occupied by B-type atoms (Mn substituted in each site with V and Fe). The other site is occupied by A-type atoms (Ti substituted with Zr).

Peak shape and positions appear to fit the collected data, as depicted in the residue graph. The main discrepancy can be found in peak intensity, despite the March-Dollase algorithm implemented to account for possible preferential orientation (the residual crushed grains may still present preferential orientation).

There's no specific literature concerning the lattice parameter for this peculiar stoichiometry, therefore a simple parallelism with $MgZn_2$ is presented. Table 3.9 shows the experimental results obtained by the XRD refinement, along with a comparison of the a/c lattice parameters ratio between our sample and the reference $MgZn_2$.
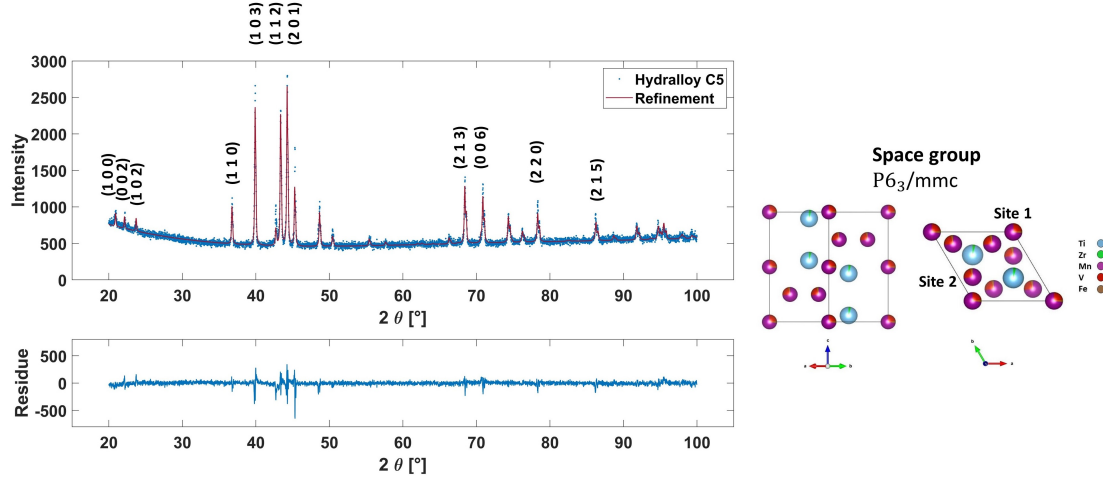
Figure 3.11: XRD powder diffraction profile and Rietveld's refinement analysis of Hydralloy C5 sample. The residue between collected data and fit is reported at the bottom of the graph. The schematic (generated by VESTA) on the right shows the crystal structure integrated into the analysis, in good agreement with the literature concerning the $MgZn_2$ or $Ti(MnV)_2$ systems [18].

	Experimental	Reference
Structure	C14 Hexagonal	C14 Hexagonal
Space group	$P6_3/mmc$	$P6_3/mmc$
a [Å]	4.8722 ± 0.0001	
c [Å]	7.9836 ± 0.0002	
a/c	0.61	0.61

Table 3.9: Hydralloy Rietveld's refinement lattice parameters compared with $MgZn_2$ Materials Project results [18].

Figure 3.12 shows the compositional map performed on the $Ti_{0.95}Zr_{0.05}Mn_{1.51}V_{0.41}Fe_{0.08}$ sample (stoichiometry written with the AB_2 nomenclature). The powder flakes appear to be homogeneous in Ti and Mn composition, with Fe-, V- and Zr-rich regions. The empty section in the middle of each elemental map is caused by the
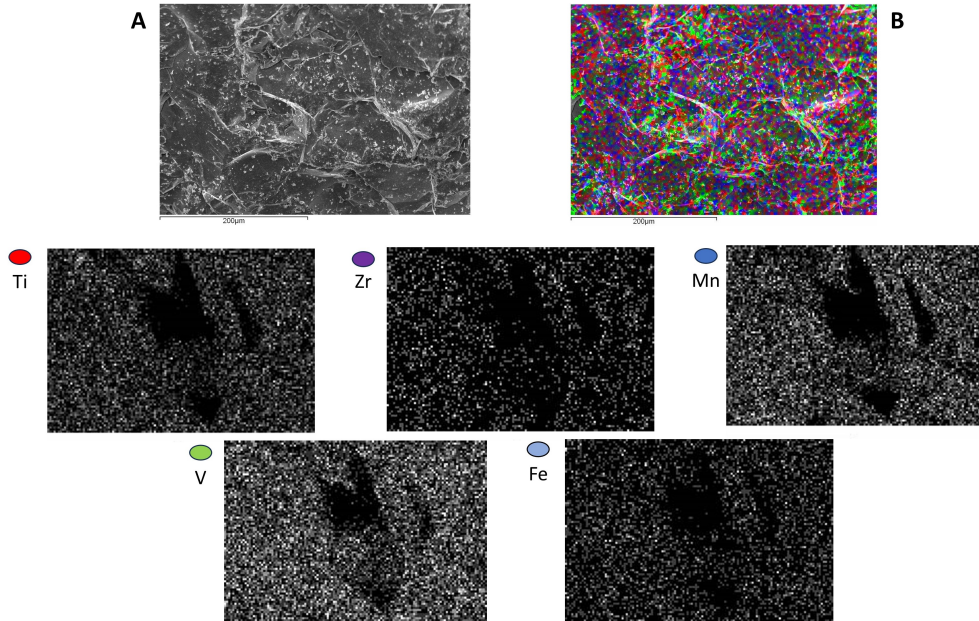
Figure 3.12: Hydralloy SEM morphological and compositional analysis at 200 *μm.*

morphological inhomogeneity on the grain surface that affects the EDX counts. Although $Mn\ K_\beta$ fluorescence is partially overlapped with $Fe\ K_\alpha$ fluorescence, thus covering part of the Fe counts in the compositional map, the results are compatible with nominal values. The elemental composition is shown in table 3.10.

	Ti	Zr	Mn	V	Fe
Nominal [at%]	30.0	1.7	50.5	14.9	2.9
Experimental [at%]	31.8 ± 0.1	1.8 ± 0.1	48.3 ± 0.5	15.1 ± 0.5	3.0 ± 0.1

Table 3.10: Nominal and SEM elemental composition for the Hydralloy C5 sample.

3.4.2 Kinetics

Figure 3.13 shows the results of a set of absorption/desorption cycles performed after sample activation. Since the equilibrium pressure for this hydride at room temperature overcomes the sensor limit of 20 bar, it was necessary to cool down the reactor below 10 °C. The temperature variation in the investigated range is too small to appreciate differences in the rate constant, although it appears that the desorption profile at $T = 17$ °C is faster than the other measurements.

Furthermore, the maximum gravimetric density, equal to $1.5 \pm 0.2\ wt\%$, appears to be smaller than the expected value (nominal value of $1.8\ wt\%$ and char-
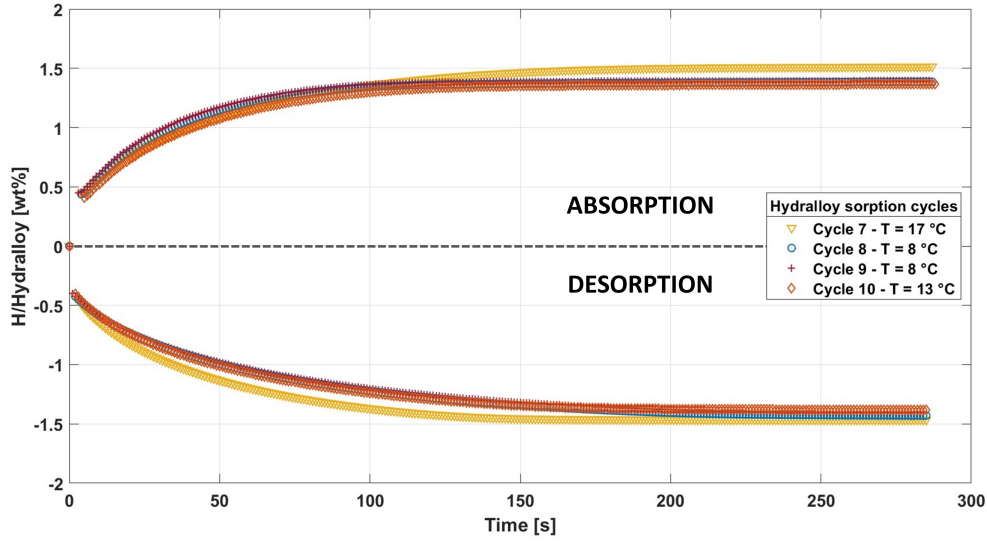
Figure 3.13: Concentration vs time profile for Hydralloy sample. The maximum gravi-metric density is equal to 1.5 ± 0.2 wt%, to be compared with the nominal value provided by the manufacturer of 1.8 wt% and with the results of [35] [36].

acterisation performed by [35] and [36]), possibly due to incomplete activation of the sample (residual surface oxides inhibiting hydrogen sorption) and to the constrained pressure range.

It is noteworthy to observe that the sorption time is compatible with the $LaNi_5$ kinetics, while discrete improvements in the total reversible gravimetric density may be reached with the AB_2 alloys. Indeed, tuning the stoichiometry of the Hydralloy C5 has brought gravimetric densities as high as 1.9 $wt\%$ [35], to be compared with the lower value of 1.4 $wt\%$ for $LaNi_5$.

3.4.3 PCIs

Figure 3.14 shows the PCIs performed on the Hydralloy sample at $T = 8, 13$ °C. As expected from the kinetic measurements, the total reversible capacity is approximately 1.6 ± 0.2 $wt\%$, a smaller value than the nominal gravimetric density declared by manufacturer and by the results of [35] [36]. As expected, a hysteresis rises at each isotherm cycle due to a thermodynamic energy barrier arising at the coherent metal/hydride interface, resulting in a different value of the chemical potential in hydrogen loading/unloading, as discussed in section 1.2.3.

Above the 1.6 $wt\%$ hydrogen concentration, the pressure in the apparatus reaches the maximum range of the sensor, precluding the possibility of exploring a higher temperature range. For this reason, it was not possible to perform a Van't

Hoff analysis in a wider T range.

The insertion graph in Figure 3.14 shows the low concentration window of the collected PCIs, where Sievert's trend, depicted in eq. (1.8), can be appreciated.
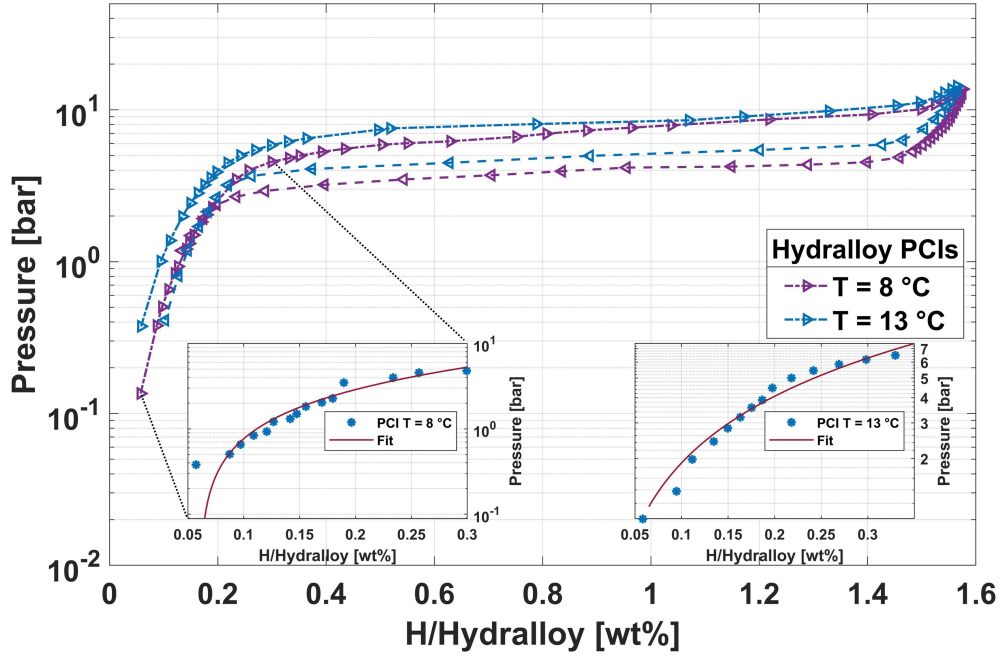
Figure 3.14: PCIs of Hydralloy sample at $T = 8, 13\ °C$, total gravimetric density equal to $1.6 \pm 0.2\ wt\%$, a value smaller than [35] [36] and the manufacturer nominal one. The inserts show the Sievert's trend in absorption for $T = 8\ °C$ (left) and $T = 13\ °C$ (right).

3.5 TiFe$_{0.9}$Ni$_{0.1}$ characterisation

3.5.1 TiFe Ball Milled

Figure 3.15 shows the diffractograms of BM TiFe powder after different milling times. Black vertical lines represent the TiFe expected peaks. The blue line at the bottom shows the presence of some peaks near the TiFe phase in the as-received powder, but the milling process has proven to be inadequate and inconvenient to form a proper TiFe phase. The amorphization process takes place as the milling time increases, eliminating any trace of TiFe crystalline phase, apart from a small peak after 21 hours of milling in a ratio ball-to-powder mass 2:1. The orange line on top shows instead the XRD profile of 8 g Ti+Fe powder in a ratio ball-to-powder mass of 2:1 after 24 hours of milling. Even when the structural composition and the amount of sample are changed, no significant variations can be appreciated,

resulting in a non-feasible procedure to synthesize TiFe. Adding ethanol to the Ar atmosphere doesn't improve the final results. Figure 3.15-B shows the same XRD profile in a narrower 2θ window, focusing on the main TiFe peak at 42.9°. As stated before, the only effect produced by the procedure is an amorphization of the initial phases (with the most intense Fe peak surviving after 24 hours) without significant formation of the TiFe phase. One possible explanation relies on the high energy deployed during the milling process, inadequate for the sample treated, a parameter different from the planetary millers found in literature [37].
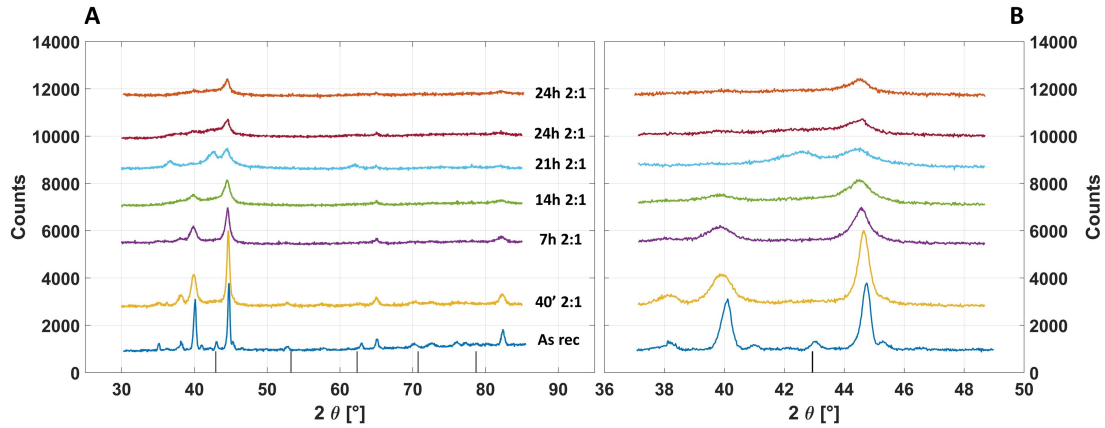
Figure 3.15: *Powder diffraction profile for 2 g TiFe at different milling time, ratio 2:1 (blue to red), and 8 g Ti+Fe 24 hours milling, ratio 2:1 (orange). Black vertical lines represent the TiFe peaks. **A)** Full range. **B)** Restricted window with major TiFe peak at 42.9°.*

3.5.2 TiFe$_{0.9}$Ni$_{0.1}$ structural and morphological characterisation

Figure 3.16 shows the powder diffraction profile of the arc-melted $TiFe_{0.9}Ni_{0.1}$ sample in the 2θ range $[25, 115]$°. Data are fitted using Rietveld's refinement analysis, and the results are shown in table 3.11. As visible in the VESTA render on the right, the cell is composed of one site for Ti and one for Fe, with partial substitution of Fe with Ni in stoichiometry 9:1. The refinement has been corrected with the March-Dollase algorithm to account for the preferential orientation of the peak at 62.1°, presumably caused by the residual large grains when crushed from the initial melted button.

In addition, it is possible to appreciate the homogeneity of the crystal structure due to the absence of spurious peaks that would have implied the presence of

66

secondary phases or impurities. The superlattice reflection at 30° instead manifests the high-order degree resulting from the arc melting technique.
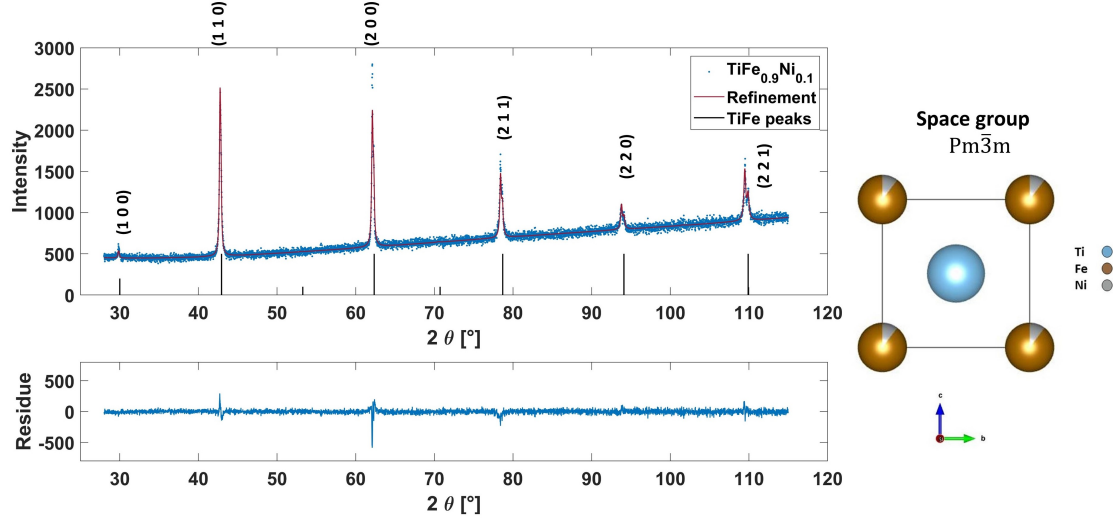
Figure 3.16: *XRD powder diffraction profile and Rietveld's refinement analysis of $TiFe_{0.9}Ni_{0.1}$ sample. The residue between collected data and fit is reported at the bottom of the graph. The schematic (generated by VESTA) on the right shows the crystal structure integrated into the analysis, in good agreement with the HighScore Plus pattern [38]. The preferred orientation peak has been refined by implementing a March-Dollase algorithm. The superlattice peak at 30° indicates a highly ordered structure, while homogeneity is ensured by the absence of spurious peaks.*

	Experimental	Reference (TiFe)
Structure	cubic	cubic
Space group	$Pm\bar{3}m$	$Pm\bar{3}m$
a [Å]	2.98204 ± 0.00002	2.976

Table 3.11: *$TiFe_{0.9}Ni_{0.1}$ Rietveld's refinement lattice parameters compared with the HighScore Plus reference on TiFe [38].*

As reported in table 3.11, the lattice parameter is compatible with the reference value regarding TiFe structure since Ni substitution doesn't significantly affect the crystal structure with this stoichiometry. The residue manifests good compatibility with data, proving that Ni substitution doesn't affect crystal structure in these stoichiometric proportions.

Figure 3.17-A shows the diffractogram collected for the $TiFe_{0.9}Ni_{0.1}$ powder after sample activation and PCI measurements in the 2θ range $[25, 115]°$. Data
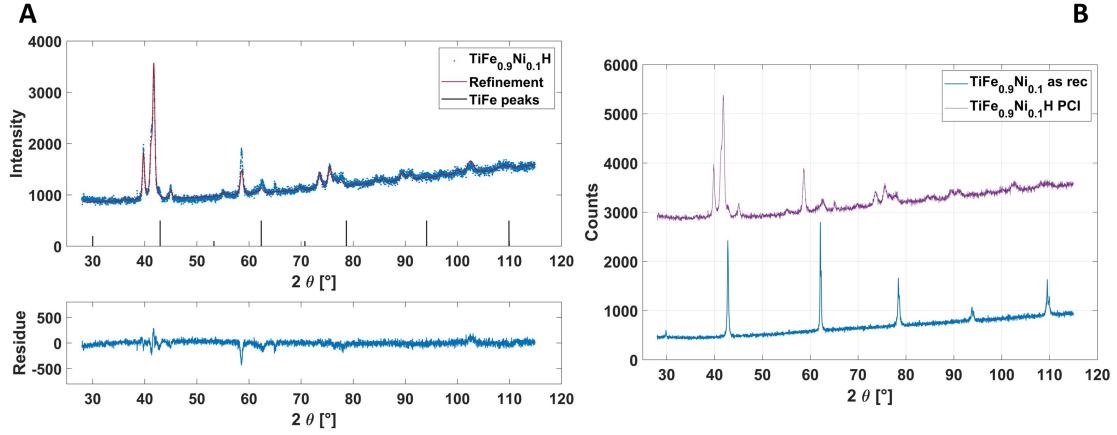
Figure 3.17: XRD powder diffraction profile of $TiFe_{0.9}Ni_{0.1}H$ sample. **A)** *Rietveld's refinement analysis and residue between the collected data and fit.* **B)** *Comparison between as received $TiFe_{0.9}Ni_{0.1}$ powder (blue line) and activated $TiFe_{0.9}Ni_{0.1}H$ mono-hydride powder (purple line).*

	Experimental	Reference
System	Orthorhombic	Orthorhombic
Space group	$P222_1$	$P222_1$
a [Å]	2.9758 ± 0.0006	2.976
b [Å]	4.5319 ± 0.0007	4.514
c [Å]	4.3788 ± 0.0006	4.378

Table 3.12: $TiFe_{0.9}Ni_{0.1}H$ Rietveld's refinement lattice parameters compared with TiFeH structure [39].

are fitted with Rietveld's refinement analysis, and the results are shown in table 3.12. The peak shape and position of the refinement fit the collected data, as visible in the residue graph. The main discrepancy can be found in the range $2\theta = 42 - 43°$, where a partial peak belonging to the non-transformed TiFe phase survives the phase transformation. Another incongruence between the model and data is represented by the peak intensity at $2\theta = 58.1°$, despite the March-Dollase algorithm integrated to account for preferential orientation. Lattice parameters (3.12) are compatible with the reference database provided by HighScore Plus [39] for *TiFeH*.

Therefore, it can be concluded that the activation and the absorption process carried out on the $TiFe_{0.9}Ni_{0.1}$ powder brought a structural transformation from *TiFe* cubic structure, space group $Pm\bar{3}m$, to orthorhombic iron titanium mono-

hydride *TiFeH*, space group $P222_1$. Figure 3.17-B shows a comparison between the as-received $TiFe_{0.9}Ni_{0.1}$ alloy and the activated powder exposed to hydrogen atmosphere. It is clear from the graph that the *TiFe* phase has completely changed to *TiFeH* mono-hydride structure.

Figure 3.18 shows the morphological (secondary-electrons detection) and compositional map (EDX micro-analysis) performed through electron microscopy on the as-received alloy. To verify the stoichiometric properties of the alloy, it was necessary to analyse the internal section of the sample, which appeared to be homogeneous in composition, validating the functionality of the arc melting technique.

Table 3.13 shows the emerging atomic ratio from elemental analysis, compared with the expected values based on the desired composition. It seems that both elemental composition and distribution satisfy the foreseen sample properties.
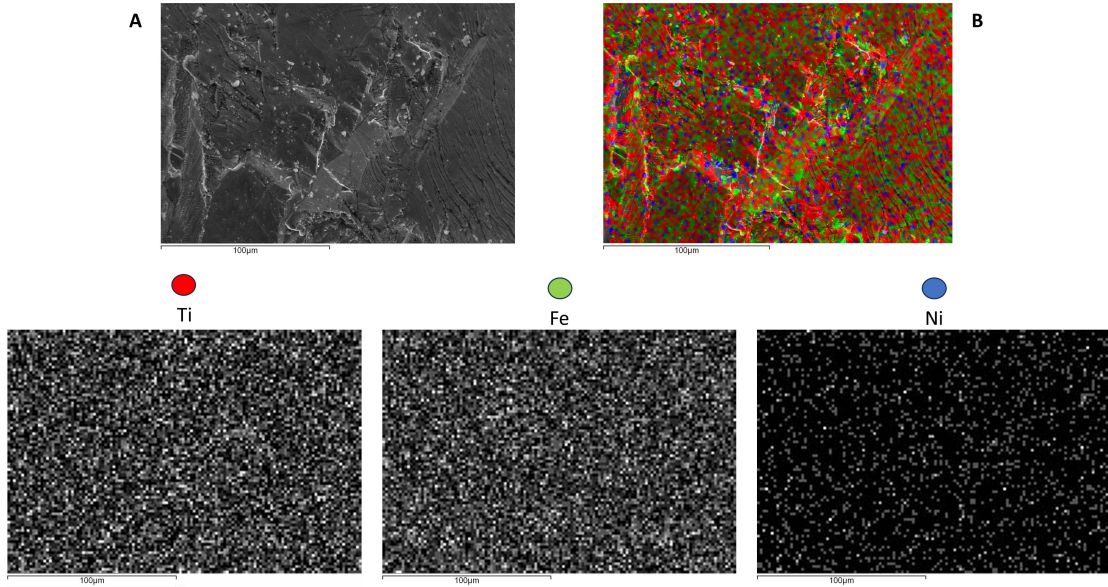
Figure 3.18: $TiFe_{0.9}Ni_{0.1}$ SEM morphological and compositional analysis of the as-melted compound.

	Experimental	Expected
Ti/Fe [at]	1.17 ± 0.01	1.11
Ti/Ni [at]	10.1 ± 0.5	10

Table 3.13: Elemental ratio (atomic percentage) of $TiFe_{0.9}Ni_{0.1}$ analysis compared with the desired stoichiometry.
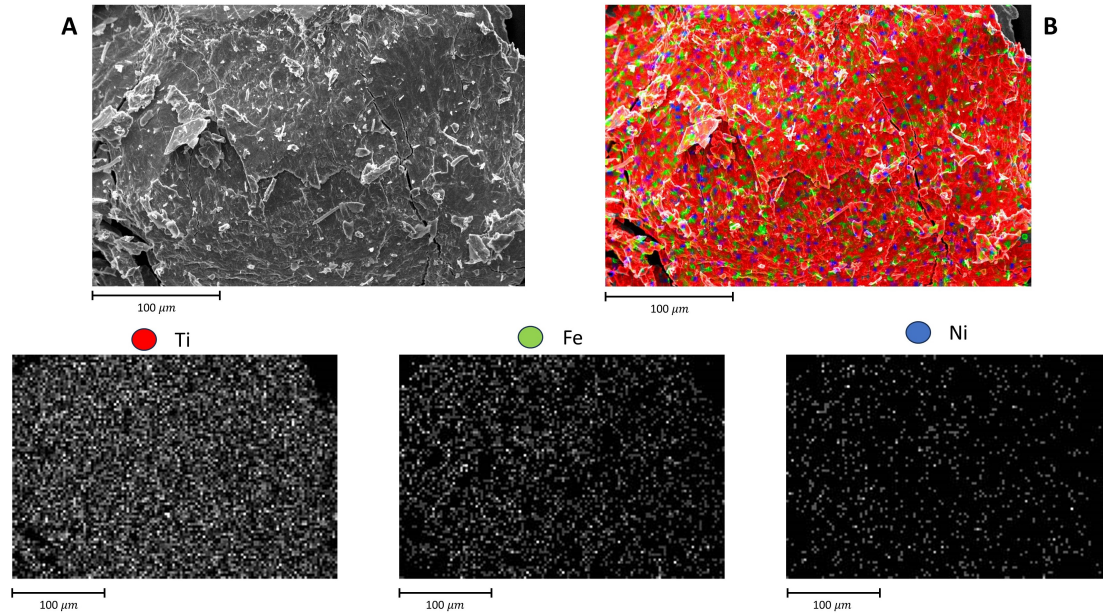
Figure 3.19: $TiFe_{0.9}Ni_{0.1}H$ SEM morphological and compositional analysis. The powder has been analysed after activation and hydrogenation cycles. It appears to be richer in Ti concentration.

Ti [at%]	Fe [at%]	Ni [at%]	Ti/Fe [at%]	Ti/Ni [at%]
55 ± 1	40 ± 1	4.6 ± 0.4	1.38 ± 0.05	12.1 ± 0.6

Table 3.14: Elemental concentration and ratio (atomic percentage) of $TiFe_{0.9}Ni_{0.1}H$ analysis.

Figure 3.19 shows the morphological and compositional analysis performed on the $TiFe_{0.9}Ni_{0.1}$ after the activation process and several sorption cycles performed. Table 3.14 lists the main results from the EDX analysis, showing an increased value in Ti concentration compared to the previous measurement. A larger amount of titanium on the powder surface may be attributed to the activation process (in particular, thermal annealing may be responsible for a re-distribution of the grains' external texture) [12].

3.5.3 Kinetics

Figure 3.20 shows the evolution of the maximum gravimetric density of the $TiFe_{0.9}Ni_{0.1}$ powder at each hydrogenation cycle. The measurements have been carried out after the activation procedure described in section 2.5.3. It is clear how the total gravimetric density increases while increasing the number of cycles, confirming the well-established idea that cycling after partial activation may benefit the material's storage capacity until it reaches its maximum value, in this case, equal to $1.25 \pm 0.08 \ wt\%$.

The seventh cycle was performed after carrying out three PCI measurements (indeed, the structure of the isotherms is distorted by the activation process occurring while the sample was absorbing hydrogen at $T = 50 \ °C$). The difference in the speed of the process is explainable by the different temperatures set during each experiment and by the kinetic processes occurring during the final activation stage despite the same external driving force set by the common initial pressure.

Notably, saturation at each cycle occurs after $200 \ s$, reflecting the fast kinetic properties manifested by the material even in mild p-T conditions, thanks to the nickel substitution performed through arc melting.
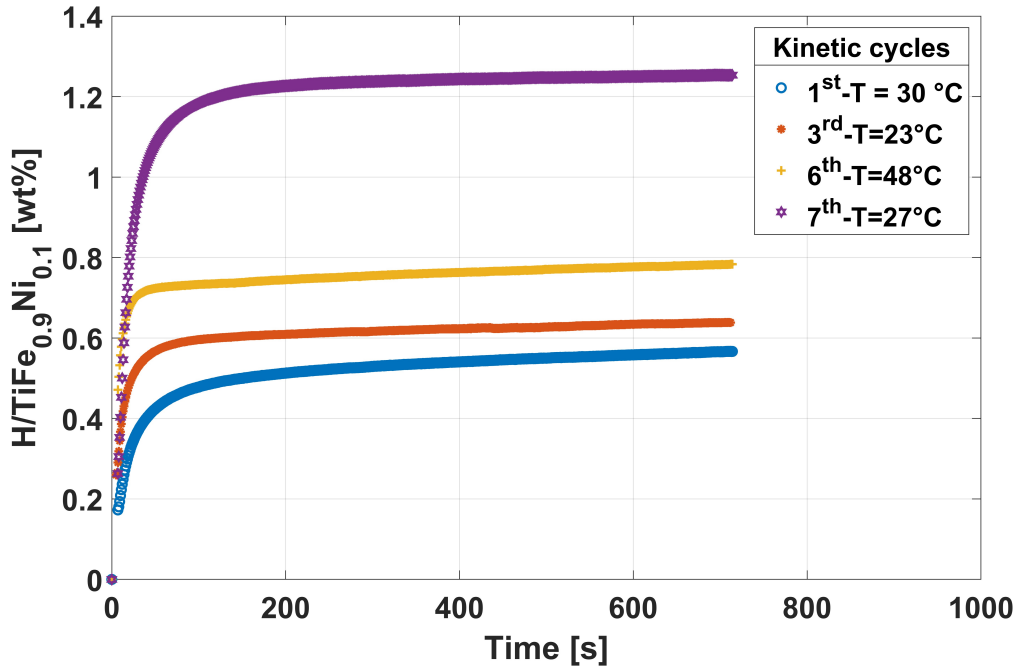
Figure 3.20: $TiFe_{0.9}Ni_{0.1}$ concentration vs time profile. The maximum gravimetric density is equal to $1.25 \pm 0.08 \ wt\%$, corresponding to the 7th cycle at $T = 27 \ °C$ (purple hexagrams). Each set of data is referred to a specific cycle of activation, performed after the procedure described in section 2.5.3.
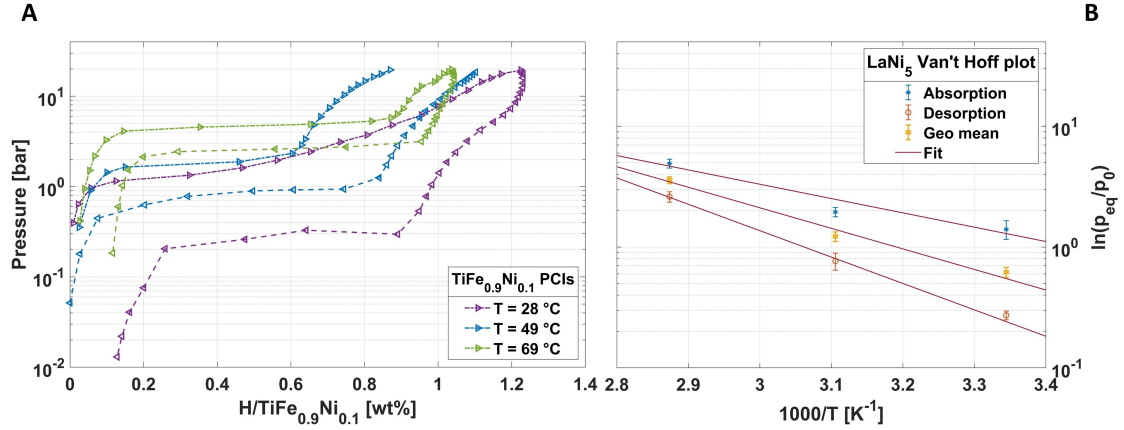
Figure 3.21: **A)** *PCIs for $TiFe_{0.9}Ni_{0.1}$ powder in the temperature range $26 - 75\ °C$. The maximum gravimetric density at $T = 26\ °C$ is $1.23 \pm 0.08\ wt\%$, in good agreement with [12] [40].* **B)** *Van't Hoff plot of the averaged plateau pressures at different temperatures. The resulting thermodynamic parameters are reported in table 3.15.*

3.5.4 PCIs and Van't Hoff plot

Figure 3.21-A shows the PCI measurements perfomed on the $TiFe_{0.9}Ni_{0.1}$ powder at $T = [26, 49, 75]\ °C$. Unfortunately, due to partial activation during measurements, the structure at 50 $°C$ appears distorted by the kinetic processes taking place in the material. Indeed, the maximum gravimetric density of $1.23 \pm 0.08\ wt\%$ manifested at room temperature reflects the complete activation of the material, confirmed by the kinetic measurement taken soon after this acquisition. Notably, the reduction of the maximum reversible capacity as temperature increases is justified by considering two factors: the expected thermodynamic behaviour of the material when T increases, and the incomplete activation of the sample when the experiments were carried out.

Figure 3.21-B shows the Van't Hoff fit performed on the absorption pressure, desorption pressure (equal to the mean value of the plateau pressures) and the geometric mean of the two. The results are shown in table 3.15, along with the enthalpy and entropy of formation of [40]. The parameters extracted from the geometric mean values seem compatible with the referenced ones, confirming the possibility of successfully tuning the thermodynamic properties of an intermetallic alloy with substitution. The discrepancy between formation and decomposition values may depend on the distorted structure of the PCIs due to incomplete activation, an effect that could have affected the accuracy in determining the plateau pressure at each temperature.

Figure 3.22 shows the equilibrium pressure-temperature curves generated by

	$\Delta H^{exp}[kJ\,mol^{-1}]$	$\Delta S^{exp}[J\,mol^{-1}\,K^{-1}]$	$\Delta H^{ref}[kJ\,mol^{-1}]$	$\Delta S^{ref}[J\,mol^{-1}\,K^{-1}]$
$\alpha \rightarrow \beta$	-23 ± 5	-78 ± 15	-31.4	-106.3
$\beta \rightarrow \alpha$	42 ± 2	128 ± 7	34.7	112.2
MEAN	32 ± 4	103 ± 13		

Table 3.15: $TiFe_{0.9}Ni_{0.1}$ Van't Hoff model parameters extracted by fitting the logarithm of the averaged plateau pressures at each temperature following eq. (1.14). The first two columns show experimental results with statistical uncertainties, while the last two lists reference data from [12] [40].

implementing in the Van't Hoff equation the enthalpy and entropy of formation of the first mono-hydride phase for pure $TiFe$ (based on Dematteis et al. [12]) compared with the experimental $TiFe_{0.9}Ni_{0.1}$ thermodynamic parameters reported in table 3.15. Notably, iron substitution through nickel significantly decreases the plateau pressure of the compound, resulting in mild p-T conditions for hydrogen sorption cycles. Particularly intriguing is the temperature interval $[0, 150]$ °C for which pressure does not overcome the 25 bar threshold.
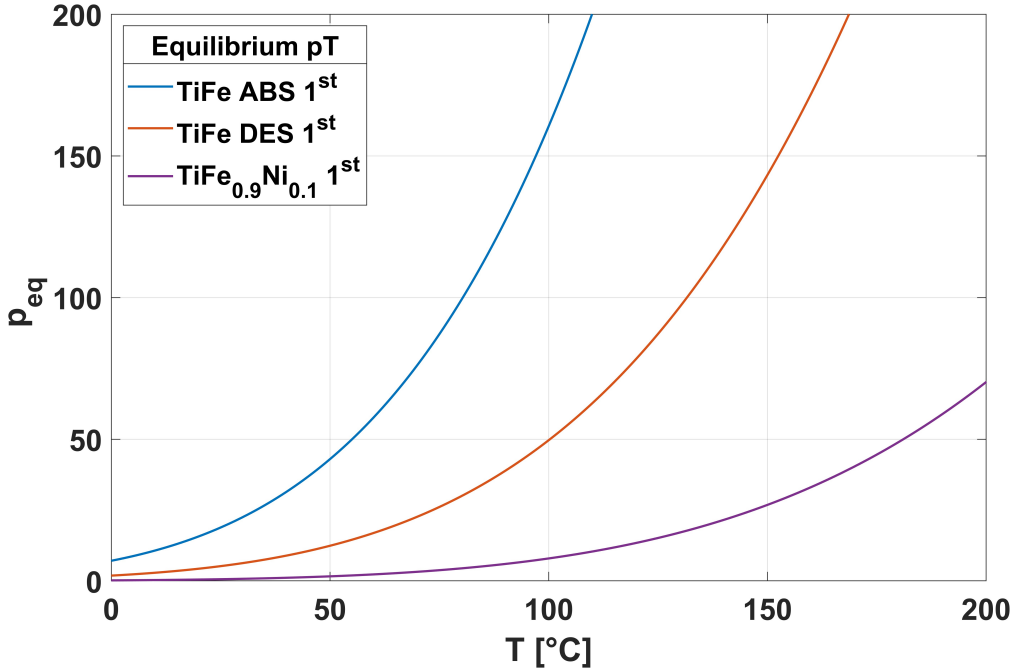

Figure 3.22: Van't Hoff (non-linearised) plot obtained by implementing enthalpy and entropy of formation (blue line) and decomposition (orange line) of the first plateau for pure TiFe (values from [12]) compared with ΔH^{exp}_{MEAN} and ΔS^{exp}_{MEAN} reported in table 3.15. A significant reduction in the mono-hydride plateau pressure can be appreciated.

Chapter 4

Conclusions

The present study was undertaken to explore viable techniques for synthesising and characterising hydride-forming compounds suitable for hydrogen storage applications.

The project is divided into two main sections:

- Calibration of a Sievert's apparatus for volumetric measurements. The system's behaviour has been modelled in pressure and temperature range to predict and analyse hydrogen sorption from intermetallic alloys. Some reference compounds (hydride-forming intermetallic alloys such as $LaNi_5H_6$ and Hydralloy C5) have been characterised through structural, morphological and compositional analysis, coupled with PCI and kinetic measurements.

- Synthesis and characterisation of novel $TiFe$ substitutions through nickel deploying the arc melting technique.

In-depth structural and morphological characterisations (Powder XRD, SE-SEM and EDX-SEM) were carried out to analyse microstructural properties and elemental composition of the materials, along with the analysis of thermodynamic and kinetic properties, including enthalpy and entropy of hydride phase formation, activation energy and rate constant. The results obtained from reference compounds are in agreement with the literature.

The Sievert's apparatus will be improved soon by implementing a new pressure sensor, increasing the operative range from the current 20 bar to a maximum value of 70 bar, allowing the exploration of a wider range of intermetallic compounds.

Throughout the project, I was able to operate an arc melter to synthesise novel intermetallic compositions for hydrogen storage applications. The potential to fine-tune the thermodynamic microscopic parameters (which directly impact the macroscopic equilibrium pressure and temperature of the hydride phases) by compositional tailoring assumes a crucial significance in material synthesis to meet

the required mild pressure and temperature operative conditions. A new arc melting device will be installed at the Department of Physics and Astronomy A. Righi in the following weeks for the synthesis of novel stoichiometry based on AB, AB_2 and AB_5 structures.

The outcomes underscore that arc melting emerges as a favourable method for synthesising intermetallic phases such as $TiFe_{0.9}Ni_{0.1}$. Indeed, the analyses notably demonstrated the benefits of employing arc melting and that the performed compositional tailoring through nickel substitution pushes the material in the desired direction: the plateau pressure has been successfully reduced compared to the $TiFe$ equilibrium pressure in the same temperature conditions, obtaining an alloy more aligned with the required p-T conditions for storage applications.

Potential directions for future investigation involve an extensive analysis of TiFeNi's stoichiometries and other intermetallic compounds. This line of research seeks to distinguish the contributions of each element in activation processes, volume expansion and contraction during cycling, and the aforementioned microscopic parameters. This comprehensive exploration aims to deepen our understanding of the interaction between hydrogen and metal hydrides, with implications for the feasibility of solid-state storage applications.

Appendix A

Raw data interpretation

The following section illustrates a general overview of the raw data collected through Sievert's apparatus. Figure A.1 shows the typical PCI acquisition in absorption (A) and desorption (B) for $m = 0.998 \pm 0.001$ g of Pd powder. The measurement is characterised by the equilibrium pressure points identified by red and yellow dots (defining the equilibrium pressure before and after opening the PV2 valve, respectively) and a series of spikes. The latter represents a simple overshoot of the system when a higher pressure in the V_{cx} section is set. The decreasing ramp is followed by the actual pressure value the operator is interested in setting in the apparatus with the PV2 closed. Subsequently, the PV2 is opened, and the pressure reaches equilibrium after a certain time interval (determined by the possible hydrogen sorption). The PV2 is closed again, allowing a pressure increment in the V_{cx} section, and then the operation is repeated. An analogous procedure has been followed for hydrogen desorption, as shown in figure A.1-B.

Figure A.2 shows the typical PCI acquisition in absorption (A) and desorption (B) for $m = 0.493 \pm 0.001$ g of $LaNi_5$ powder. The same p1 and p2 (red and yellow dots) are reported, along with the pressure points calculated from the ideal gas equation (purple circle), representing the expected pressure the apparatus should reach whenever the PV2 is opened and before any hydrogen sorption event. As clear from the graph, the system behaves following this model, confirming the validity of the background measurements performed as a preliminary analysis.

Figure A.3 shows the pressure vs time profile for $m = 0.493 \pm 0.001$ g of $LaNi_5$ sample for absorption (A) and desorption (B) at $T = 49$ °C. Each insertion shows a close-up of the "exponential" profile, which reflects the hydrogen sorption process. Each time-pressure window has been fitted following eq. (2.9) (2.10). The same data has been manipulated and linearised to apply the logarithmic version of the JMAK model. It is possible to appreciate the undershoot of the pressure measurement (figure A.3-A) when the system goes from 17 to 15 bar. Since the reactor side of the apparatus is in vacuum during absorption kinetics, a severe
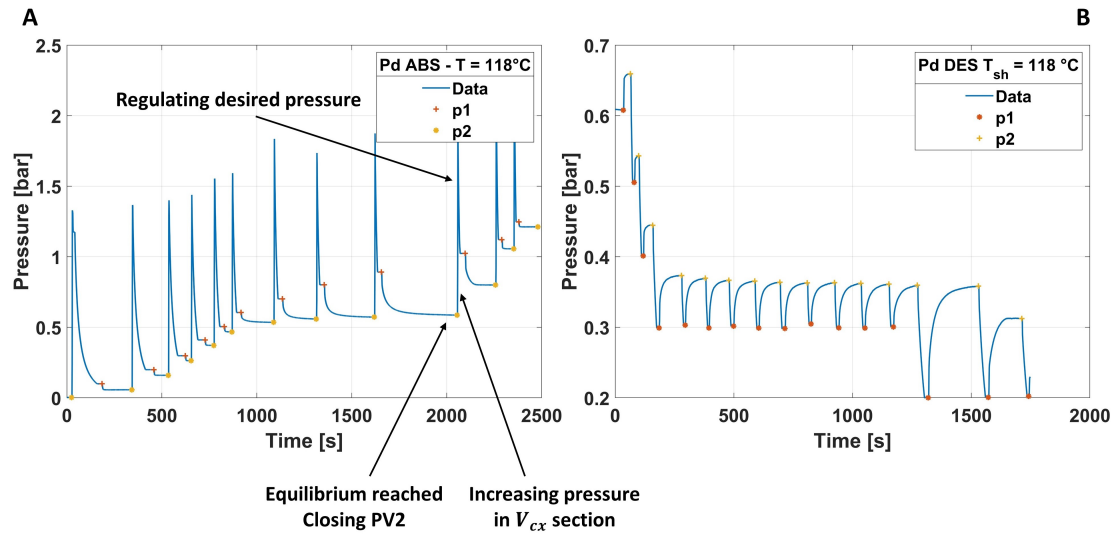
Figure A.1: PCI raw data for Pd sample at T = 118 °C. **A)** *Absorption data. The spikes represent an overshoot of the apparatus when setting the desired pressure. Red and yellow dots identify the equilibrium pressure before and after opening the PV2 valve.* **B)** *Desorption data.*

pressure variation may result in a non-ideal system behaviour. This trend has been accounted for when evaluating the variation in the number of moles.
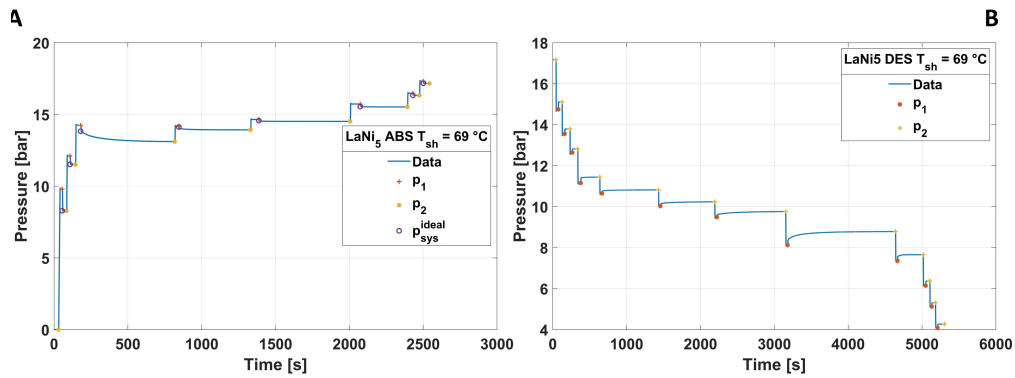
Figure A.2: PCI raw data for $LaNi_5$ sample at T = 69 °C. **A)** *Absorption data. Red and yellow dots identify the equilibrium pressure before and after opening the PV2 valve. At the same time, the purple circles represent the expected pressure calculated with the ideal gas model without hydrogen sorption.* **B)** *Desorption data.*

Table A.1, A.2,A.3 and A.4 show the equilibrium pressure values for Pd, $LaNi_5$ Hydralloy C5 and $TiFe_{0.9}Ni_{0.1}$ samples, respectively.

T [$^{\circ}C$]	p_{abs} [bar]	p_{des} [bar]	p_{mean} [bar]
118	0.58 ± 0.02	0.37 ± 0.01	0.46 ± 0.01
150	1.39 ± 0.06	1.0 ± 0.1	1.20 ± 0.09
201	4.06 ± 0.07	3.7 ± 0.3	3.9 ± 0.2
241	8.2 ± 0.2	7.3 ± 0.3	7.7 ± 0.2
281	15.0 ± 0.3	15.0 ± 0.2	15.0 ± 0.2

Table A.1: Pd pressure-temperature value in absorption, desorption and geometric mean.

T [$^{\circ}C$]	p_{abs} [bar]	p_{des} [bar]	p_{mean} [bar]
28	3.1 ± 0.8	2.0 ± 0.3	2.5 ± 0.4
49	6.9 ± 0.9	5 ± 1	6.0 ± 0.9
69	13 ± 1	10 ± 2	11 ± 1

Table A.2: $LaNi_5$ pressure-temperature value in absorption, desorption and geometric mean.

T [$^{\circ}C$]	p_{abs} [bar]	p_{des} [bar]	p_{mean} [bar]
8	7 ± 2	4 ± 1	5 ± 1
13	7 ± 3	4.5 ± 0.9	5 ± 1

Table A.3: Hydralloy C5 pressure-temperature value in absorption, desorption and geometric mean.

T [$^{\circ}C$]	p_{abs} [bar]	p_{des} [bar]	p_{mean} [bar]
26	1.5 ± 0.5	0.27 ± 0.05	0.6 ± 0.1
49	1.9 ± 0.3	0.8 ± 0.2	1.2 ± 0.2
75	4.9 ± 0.8	2.6 ± 0.5	3.5 ± 0.4

Table A.4: $TiFe_{0.9}Ni_{0.1}$ pressure-temperature value in absorption, desorption and geometric mean.

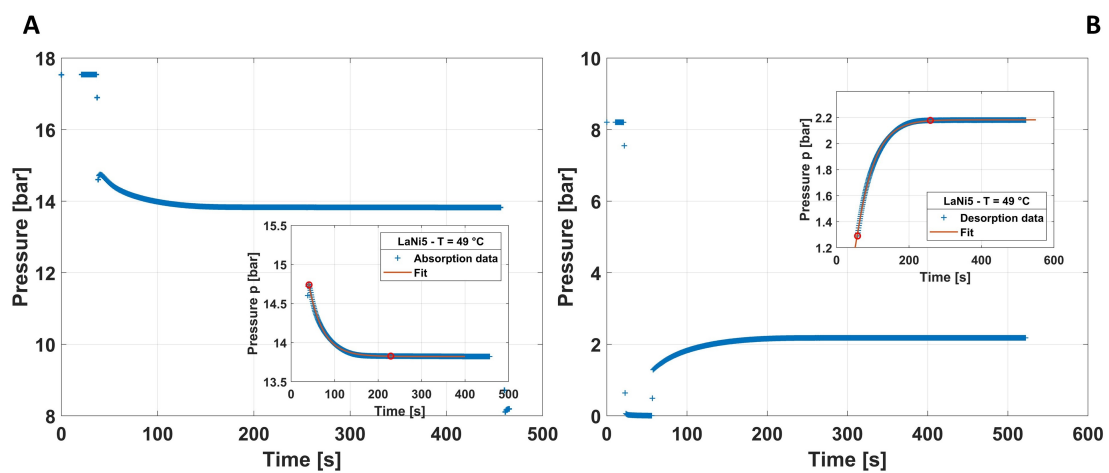*Figure A.3: Kinetic profile for LaNi$_5$ sample at $T = 49$ °C.* **A)** *Absorption profile. The insertion shows the absorption process with the fit window identified by the red dots.* **B)** *Desorption profile. The insertion shows the desorption process with the fit window identified by the red dots.*

References

[1] L. Pasquini, "Design of nanomaterials for hydrogen storage", Energies **13** (2020).

[2] L. Pasquini and K. S. et al., "Magnesium- and intermetallic alloys-based hydrides for energy storage: modelling, synthesis and properties", Progress in Energy **4**, 032007 (2022).

[3] F. P. Jose M Bermudez Stavroula Evangelopoulou, "Hydrogen - energy system overview", (2022).

[4] M. Kayfeci, A. Keçebaş, and M. Bayat, "Chapter 3 - hydrogen production", in *Solar hydrogen production*, edited by F. Calise, M. D. D'Accadia, M. Santarelli, A. Lanzini, and D. Ferrero (Academic Press, 2019), pp. 45–83.

[5] B. A. Züttel A Remhof A, *Hydrogen: the future energy carrier* (2010).

[6] S. Mekhilef, R. Saidur, and A. Safari, "Comparative study of different fuel cell technologies", Renewable and Sustainable Energy Reviews **16**, 981–989 (2012).

[7] A. Züttel, "Fuels – hydrogen storage, hydrides", Encyclopedia of Electrochemical Power Sources, edited by J. Garche, 440–458 (2009).

[8] R. Kirchheim and A. Pundt, "25 - hydrogen in metals", in *Physical metallurgy (fifth edition)*, edited by D. E. Laughlin and K. Hono, Fifth Edition (Elsevier, Oxford, 2014), pp. 2597–2705.

[9] Y. Fuaki, *The metal-hydrogen system*, 2nd ed. (Springer Berlin, Heidelberg).

[10] R. Schwarz and A. Khachaturyan, "Thermodynamics of open two-phase systems with coherent interfaces: application to metal–hydrogen systems", Acta Materialia **54**, 313–323 (2006).

[11] "A correlation between the interstitial hole sizes in intermetallic compounds and the thermodynamic properties of the hydrides formed from those compounds", Journal of the Less Common Metals **56**, 19–37 (1977).

[12] E. M. Dematteis, N. Berti, F. Cuevas, M. Latroche, and M. Baricco, "Substitutional effects in tife for hydrogen storage: a comprehensive review", Mater. Adv. **2**, 2524–2560 (2021).

¹³W. C. C. Robert W. Balluffi Sam Allen, *Kinetics of materials* (Wiley, 2005).

¹⁴M. H. Mintz and Y. Zeiri, "Hydriding kinetics of powders", Journal of Alloys and Compounds **216**, 159–175 (1995).

¹⁵Z. S. W. Robert A. Varin Tomasz Czuijko, "Nanomaterials for hydrogen storage", in *Fuel cells and hydrogen energy*, edited by D. E. Laughlin and K. Hono, Third Edition (Springer, 2009).

¹⁶L. Q. e. a. Li Q. Lin X., "Kinetics of the hydrogen absorption and desorption processes of hydrogen storage alloys: a review.", Int J Miner Metall Mater, `https://doi.org/10.1007/s12613-021-2337-8` (2022).

¹⁷E. Kisi, C. Buckley, and E. Gray, "The hydrogen activation of lani5", Journal of Alloys and Compounds **185**, 369–384 (1992).

¹⁸`https://next-gen.materialsproject.org/`.

¹⁹S. K. Pandey, A. Srivastava, and O. Srivastava, "Improvement in hydrogen storage capacity in lani5 through substitution of ni by fe", International Journal of Hydrogen Energy **32**, ICHS-2005, 2461–2465 (2007).

²⁰G. Cacciamani, J. De Keyzer, R. Ferro, U. Klotz, J. Lacaze, and P. Wollants, "Critical evaluation of the fe–ni, fe–ti and fe–ni–ti alloy systems", Intermetallics **14**, EUROMAT 2005 "European Congress on Advanced Materials and Processes", 1312–1325 (2006).

²¹H. Okamoto, "Supplemental literature review of binary phase diagrams: al-pt, as-u, c-li, c-mg, cd-nd, co-ta, fe-re, ga-y, la-ni, o-v, p-si, and re-zr.", J. Phase Equilib. Diffus., `https://doi.org/10.1007/s11669-020-00839-9` (2020).

²²P. Riani, G. Cacciamani, Y. Thebaut, and J. Lacaze, "Phase equilibria and phase transformations in the ti-rich corner of the fe–ni–ti system", Intermetallics **14**, EUROMAT 2005 "European Congress on Advanced Materials and Processes", 1226–1230 (2006).

²³G. Sandrock, "A panoramic overview of hydrogen storage alloys from a gas reaction point of view", Journal of Alloys and Compounds **293-295**, 877–888 (1999).

²⁴P. Jain, C. Gosselin, and J. Huot, "Effect of zr, ni and zr7ni10 alloy on hydrogen storage characteristics of tife alloy", International Journal of Hydrogen Energy **40**, Special issue on 1st International Conference on Hydrogen Storage, Embrittlement and Applications (Hy-SEA 2014), 26-30 October 2014, Rio de Janeiro, Brazil, 16921–16927 (2015).

²⁵Y.-W. Lee, B. Clemens, and K. Gross, "Novel sieverts' type volumetric measurements of hydrogen storage properties for very small sample quantities", Journal of Alloys and Compounds - J ALLOYS COMPOUNDS **452**, 410–413 (2008).

[26] https://www.swagelok.com (visited on 06/15/2023).

[27] https://www.malvernpanalytical.com/en/products/category/software/x-ray-diffraction-software/highscore-with-plus-option.

[28] https://luttero.github.io/maud/.

[29] https://jp-minerals.org/vesta/en/.

[30] M. Yamauchi, H. Kobayashi, and H. Kitagawa, "Hydrogen storage mediated by pd and pt nanoparticles", ChemPhysChem **10**, 2566–2576.

[31] R. Lässer and K. H. Klatt, "Solubility of hydrogen isotopes in palladium", Phys. Rev. B **28**, 748–758 (1983).

[32] https://www.malvernpanalytical.com/en/products/category/software/x-ray-diffraction-software/highscore-with-plus-option,ref-code=00-012-0497.

[33] S. P. H. K. S. NAHM W. Y. KIM and W. Y. LEE, "The reaction kinetics of hydrogen storage in lani5", Int. J Hydrogen Energy (1992).

[34] D. Ohlendorf and H. E. Flotow, "Heat capacities and thermodynamic functions of lani5, lani5h0.36 and lani5h6.39 from 5 to 300 k", Journal of the Less Common Metals **73**, 25–32 (1980).

[35] M. Kölbig, I. Bürger, and M. Linder, "Characterization of metal hydrides for thermal applications in vehicles below 0 °c", International Journal of Hydrogen Energy **44**, 4878–4888 (2019).

[36] M. Kölbig, I. Bürger, and M. Linder, "Thermal applications in vehicles using hydralloy c5 in single and coupled metal hydride systems", Applied Energy **287**, 116534 (2021).

[37] E. O. e. a. Hosni B. Fenineche N., "Structural and electrochemical properties of tife alloys synthesized by ball milling for hydrogen storage", J Solid State Electrochem **22**, https://doi.org/10.1007/s10008-017-3718-9 (2017).

[38] https://www.malvernpanalytical.com/en/products/category/software/x-ray-diffraction-software/highscore-with-plus-option,ref-code=00-019-0636.

[39] https://www.malvernpanalytical.com/en/products/category/software/x-ray-diffraction-software/highscore-with-plus-option,ref-code=00-026-0806.

[40] M. Mintz, S. Vaknin, S. Biderman, and Z. Hadari, "Hydrides of ternary tifem intermetallics", Journal of Applied Physics **52**, 463–467 (1981).